Wave Forcing: Towards Speed-of-Light Streaming Video Generation

Yijie Jin[1†] **Yuxuan Liu**[1†] **Jiajun Xu**[1,2†] **Ye Huang**[3†] **Chuzhi Wang**[1]
Jiayang Li[4] **Ruiyang Chen**[1] **Chenling Hong**[5] **Xu Wang**[1] **Zhijie Deng**[1‡]

[1]DENG Lab, Shanghai Jiao Tong University
[2]Xi'an Jiaotong University [3]Peking University
[4]East China Normal University [5]National Tsing Hua University

{drewjin0827, liuyx2005, zhijied}@sjtu.edu.cn
mikanaffine@stu.xjtu.edu.cn, huangye26@stu.pku.edu.cn

GitHub Project Page Hugging Face

arXiv:2611.00859v1 [cs.CV] 31 Oct 2026

Abstract

Real-time long-video generation requires continuous output with consistent appearance and natural motion. Existing chunk-wise autoregressive methods face challenges in both generation efficiency and long-video quality: serialized denoising and history-cache refresh require two forward passes even with one-step denoising, and longer rollouts can degrade quality and cause camera drift. We propose **Wave Forcing (WF)**, which co-designs generation, training, and execution for continuous video output with multi-step denoising. WF uses chunk-wise causal attention to access earlier, cleaner chunks before their denoising is complete, and distributes staggered denoising and cache-refresh stages across full-model replicas to achieve **1F1C**: one output chunk per concurrent forward round after pipeline fill. To adapt the model to this continuous generation process, we develop a three-stage training procedure that successively introduces mixed-noise denoising, motion supervision, and causal adaptation using self-generated history. To execute this process efficiently, **Wave Runtime (WaveRT)** uses **Wave Parallelism (WP)** for early K/V delivery and communication–computation overlap, together with optimized kernels and pipelined VAE decoding. Experiments on Wan2.1-T2V-1.3B show that 5-step WF maintains overall quality comparable to Rolling Forcing while achieving higher Dynamic Degree on both short and long videos. Our system efficiency experiments show that 4-step WF achieves **147.6 DiT FPS** and **134.8 end-to-end FPS** on eight H200 GPUs, yielding **7.07**× the single-GPU end-to-end throughput. In DiT-only tests with matched SageAttention+W8A8 backends, denoising steps, and GPU counts, WP delivers up to **2.53**× the throughput of the faster of the Ulysses and Ring context-parallel baselines across six model scales (1.3B–14B).

1 Introduction

Real-time streaming video generation must sustain playable output with consistent appearance and natural motion. Chunk-wise autoregressive methods such as Self Forcing (SF) and Causal Forcing (CF) denoise each chunk conditioned on preceding content (Huang et al., 2025a; Zhu et al., 2026b). Under the clean-history caching convention adopted in this work, an additional forward pass, termed *store*, refreshes the key/value (K/V) history from the clean result. Sequential execution places denoising and store between consecutive outputs, yielding **NF1C (N Forward Rounds, 1 Chunk Output)**. Thus, even one-step denoising requires two forward passes when store is included.

We target **1F1C**: one completed chunk per concurrent forward round after pipeline fill, while retaining every denoising update. Inspired by wavefront scheduling (Jin et al., 2016), earlier chunks execute later denoising stages while newer chunks execute earlier ones. These staggered tasks form a moving *wavefront* (Fig. 1a). Assigning a full-model replica to each denoising stage and the store stage creates a bounded-width pipeline (Fig. 1c).

To advance chunks before their predecessors finish, we use *chunk-wise causal context*: full attention within each chunk, cached history, and live context from earlier, cleaner chunks, with no dependence

[†]Equal contribution.
[‡]Corresponding author.

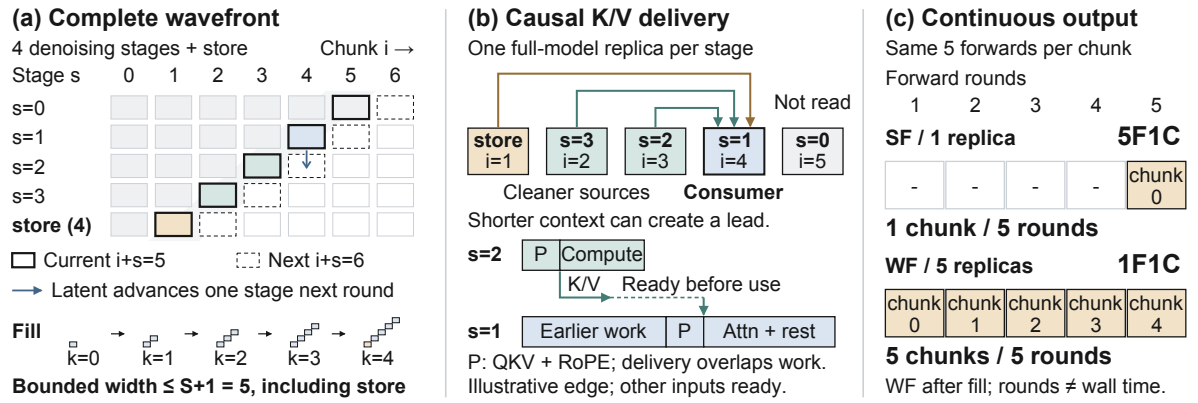


Figure 1: Causal wavefront and continuous output ($S = 4$). (a) Denoising and store advance on anti-diagonals, with dashed cells marking the next round. (b) One later-layer K/V edge arrives before use. Other edges and initial waits are omitted. (c) Both schedules retain four denoising forwards plus store per chunk. Over five rounds, one SF replica emits one chunk, whereas five WF replicas emit five after fill. Wall-clock gains depend on stage costs and overlap.

on later chunks. This directional conditioning accommodates differences in stage-wise progress and enables overlapped execution (Fig. 1b). Our staged training builds on mixed-noise joint denoising (Liu et al., 2026), uses teacher videos to supervise motion and framing, and adapts the model to causal inference with self-generated history. This generation structure and its training recipe together constitute **Wave Forcing (WF)**.

To turn this scheduling potential into shorter output intervals, **Wave Runtime (WaveRT)** implements **Wave Parallelism (WP)**. Following GPU software-pipelining principles (NVIDIA, 2026a;b), WP exploits differences in stage-wise progress for early layer-wise K/V delivery and communication–computation overlap, reducing exposed dependency waits. Data placement, kernel optimization, and load-balanced VAE pipeline parallelism complete the execution path from concurrent denoising to sustained video output.

On Wan2.1-T2V-1.3B (Wan et al., 2025), 5-step WF achieves overall quality comparable to 5-step Rolling Forcing (RF), with VBench Total scores of 81.64 versus 81.15 and VBench-Long Quality scores of 81.26 versus 81.18 (Huang et al., 2024; 2026b). Dynamic Degree increases from 51.39 to 94.44 on short videos and from 36.63 to 91.45 on 100-second videos. These gains are accompanied by better Subject Preservation (97.10 versus RF's 92.75) while maintaining low Camera Drift (0.37 versus RF's 0.17).

In terms of system performance, 4-step WF with the BF16/FA3 backend achieves **147.6 DiT FPS** and **134.8 end-to-end FPS** on eight H200 GPUs, yielding a **7.07**× end-to-end speedup over the 19.06-FPS single-GPU baseline (Table 4). At this denoising speed, residual output-path overhead remains visible even with three-stage VAE pipelining, as discussed in Section 7. Across six model scales from 1.3B to 14B, WP outperforms the faster context-parallel (CP) baseline at five scales under BF16 and all six under Sage+W8A8, achieving **1.025–2.530**× its throughput under Sage+W8A8. System ablations and profiling further analyze how communication overlap, K/V placement, compute backends, and VAE stage balance affect runtime performance.

Our contributions are threefold:

- **Causal wavefront generation.** We introduce Wave Forcing, allowing newer chunks to condition on earlier, cleaner chunks before their denoising completes. By pipelining denoising and clean-history cache refresh across full-model replicas, WF enables one completed chunk per concurrent forward round (1F1C) after pipeline fill while retaining all denoising updates.
- **Training for continuous generation.** We develop a staged training recipe combining mixed-noise initialization, teacher-guided motion supervision, and causal adaptation with self-generated history. This adapts the model to wavefront inference, enabling strong motion and subject preservation over long rollouts at overall quality comparable to Rolling Forcing.
- **Efficient streaming execution.** We build Wave Runtime to realize wavefront concurrency through early layer-wise K/V delivery, communication–computation overlap, and direct placement into attention buffers. With optimized local computation and load-balanced VAE decoding, the runtime translates stage concurrency into sustained end-to-end throughput, with efficiency validated across 1.3B–14B models.

2 Preliminaries

Chunk denoising and store. A VAE decodes latent-frame chunks into video (Wan et al., 2025). Following SF (Huang et al., 2025a), chunk i undergoes S history-conditioned denoising updates, from noise $Z_i^{(0)}$ to clean output $B_i = Z_i^{(S)}$. At noise timesteps $\nu_0 > \cdots > \nu_S = 0$,

$$Z_i^{(s+1)} = \Psi_{\nu_{s+1}}\left(G_\theta(Z_i^{(s)}, \nu_s \mid \mathcal{C}_{i,s}), \epsilon_{i,s}\right), \qquad 0 \le s < S, \tag{1}$$

G_θ predicts clean latents, which Ψ_ν re-noises using draw $\epsilon_{i,s}$, with $\Psi_0(x, \epsilon) = x$. $\mathcal{C}_{i,s}$ denotes layer-wise K/V context, with text conditioning omitted for brevity. Denoising K/V represents the noisy input, so our clean-history convention adds *store*: a full-model forward on B_i that retains K/V and discards the prediction. Sequential generation thus uses $N = S + 1$ forwards per chunk (NF1C).

Wavefront states and execution rounds. At filled runtime tick k, the denoising inputs are

$$\mathcal{F}_k = \{Z_k^{(0)}, Z_{k-1}^{(1)}, \ldots, Z_{k-S+1}^{(S-1)}\}. \tag{2}$$

Adding store at $s = S$ gives $\mathcal{W}_k = \mathcal{F}_k \cup \{B_{k-S}\}$, of width at most $S + 1$ excluding anchor/history caches. Each round advances active stages and admits fresh noise. With stage-owned replicas, this schedule permits 1F1C after fill without changing per-chunk work.

3 Wave Forcing

We introduce **Wave Forcing (WF)** to advance successive chunks before their predecessors finish denoising. WF couples a causal wavefront—newer, noisier chunks read earlier, cleaner states, but not vice versa—with training for this mixed-noise context and self-generated history.

3.1 A bounded-width causal wavefront

Cell (i, s), $s < S$, in Fig. 1a updates $Z_i^{(s)}$ to $Z_i^{(s+1)}$ in round

$$k = i + s, \qquad i = k - s. \tag{3}$$

Store at $(k - S, S)$ refreshes B_{k-S}'s K/V. For N_{chunk} requested chunks, active denoising stages are $\mathcal{A}_k = \{s : 0 \le s < S,\ 0 \le k - s < N_{\text{chunk}}\}$. Store is active when $0 \le k - S < N_{\text{chunk}}$.

WF retains full attention within each chunk and uses *chunk-wise causal attention* across video time. Query slot s sees K/V slot j iff

$$M_{\text{WF}}(s, j) = \mathbf{1}[j \ge s], \qquad s, j \in \mathcal{A}_k. \tag{4}$$

In chunk order, $i' = k - j \le i = k - s$ gives a lower-triangular mask over self and *all* cleaner predecessors.

At Transformer layer $\ell \in \{1, \ldots, L\}$, the ordered context is

$$\mathcal{C}_{k,s}^{\text{WF},\ell} = A_k^\ell \oplus H_k^\ell \oplus U_k^\ell \oplus \Big[\bigoplus_{\substack{j \in \mathcal{A}_k \\ j \ge s}} (K_{k,j}^\ell, V_{k,j}^\ell)\Big], \tag{5}$$

Here $\oplus$ concatenates initial-chunk anchor A_k^ℓ, bounded clean history H_k^ℓ, live store U_k^ℓ, and denoising K/V in increasing j (self first). Store appears once, is empty when inactive, and enters history after the round. Appendix B details fill/drain and caching.

This removes Rolling Forcing's (RF) reverse refinement (Liu et al., 2026). Without post-training, short-video Quality and Dynamic Degree fall in our evaluation (Sec. 5.1), motivating adaptation.

3.2 Training for the deployment graph

The causal mask removes access to later, noisier active chunks, changing RF's learned conditioning. We adapt Wan2.1-T2V-1.3B (Wan et al., 2025) through mixed-noise initialization, teacher guidance, and on-policy training (Fig. 2). The 4-step student starts from SF's ODE initialization, whereas the 5-step student reuses released RF weights and skips Stage 1.

Stage 1: mixed-noise initialization. We adopt RF's mixed-noise joint-denoising setup (Liu et al., 2026), using bidirectional attention across chunks at different noise levels. We sample either an RF rollout or an SF rollout with equal probability and train the student with distribution matching distillation (DMD) (Yin et al., 2024). SF rollouts help stabilize motion during initialization.

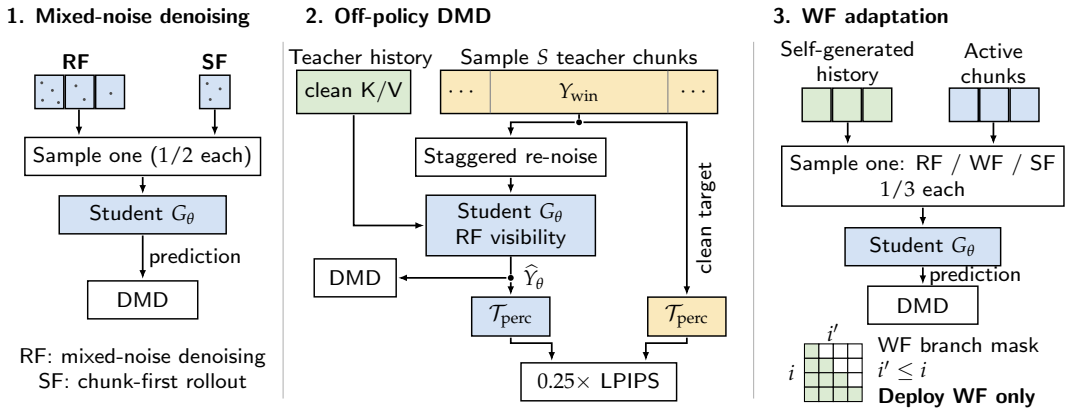


Figure 2: Training flow. Stage 1 applies DMD to one sampled RF or SF rollout. Stage 2 re-noises teacher chunks and applies DMD and LPIPS to the same prediction $\widehat{Y}_\theta$. Stage 3 samples one self-generated RF, WF, or SF rollout for on-policy DMD.

Stage 2: off-policy DMD. Following LPM 1.0 (Zeng et al., 2026), we re-noise consecutive teacher chunks Y_{win} at staggered timesteps, with preceding teacher chunks as clean K/V history. Retaining Stage 1's bidirectional attention, this supplies stronger motion and subject guidance (Sec. 5.2). DMD and LPIPS (Zhang et al., 2018) supervise the same text-conditioned prediction $\widehat{Y}_\theta$:

$$\mathcal{L}_2 = \mathbb{E}\Big[\mathcal{D}_{\text{DMD}}(\widehat{Y}_\theta; \mathbf{c}) + \lambda_{\text{p}}\,\text{LPIPS}\Big(\mathcal{T}_{\text{perc}}(\widehat{Y}_\theta), \mathcal{T}_{\text{perc}}(Y_{\text{win}})\Big)\Big], \qquad \lambda_{\text{p}} = 0.25, \tag{6}$$

Here $\mathcal{D}_{\text{DMD}}$ is the DMD objective, and $\mathcal{T}_{\text{perc}}$ decodes downsampled latents to sampled RGB frames.

Stage 3: causal context and self-generated history. Each iteration uniformly samples a self-generated RF, WF, or SF rollout for on-policy DMD. WF uses Eq. (5), including store-refreshed history from its own outputs. RF and SF provide complementary training distributions, but only WF is deployed. For branch objective $\mathcal{L}_b$,

$$\mathcal{L}_3 = \mathbb{E}_{b\sim\text{Unif}\{\text{RF,WF,SF}\}}[\mathcal{L}_b] = \tfrac{1}{3}\mathcal{L}_{\text{RF}} + \tfrac{1}{3}\mathcal{L}_{\text{WF}} + \tfrac{1}{3}\mathcal{L}_{\text{SF}}. \tag{7}$$

Appendix A gives stage transitions and implementation details. Together, these stages adapt the model to causal wavefront inference: chunks denoise using cleaner, still-evolving predecessors and self-generated history.

4 Wave Runtime

WF exposes stage concurrency, but K/V dependencies can still stall attention. **Wave Runtime (WaveRT)** realizes **Wave Parallelism (WP)** by publishing K/V early from stage-owned replicas and overlapping delivery with computation when cleaner producers run ahead. We use SGLang Diffusion's model implementation as the core execution backend (Zheng et al., 2024) of WaveRT.

4.1 Stage placement and dependencies

Each denoising stage and store owns a full-model GPU replica. Denoising rank s updates $Z_{k-s}^{(s)}$ and passes it to rank $s+1$ for the next round (Fig. 1). Within a round, let $P_{s,\ell}$ produce Q/K/V and RoPE, and $C_{s,\ell}$ perform attention and the remaining block:

$$P_{s,\ell} \to C_{s,\ell}, \qquad C_{s,\ell} \to P_{s,\ell+1} \quad (\ell < L), \tag{8}$$

$$P_{j,\ell} \to C_{s,\ell}, \qquad j > s, \quad s, j \in \mathcal{A}_k. \tag{9}$$

At each layer, local projection can proceed without waiting for remote K/V, but attention must wait until store and all legal cleaner ranks, including nonadjacent ranks, have supplied their K/V. RF additionally depends on noisier ranks, introducing reverse edges that WF removes through its causal mask. The synchronized reference enforces these dependencies with a per-layer all-rank K/V gather.

4.2 Producer lead and asynchronous delivery

In a filled round, rank s reads N_C query tokens and N_s keys, where

$$N_s = N_{\text{prefix}} + (S - s)N_C. \tag{10}$$

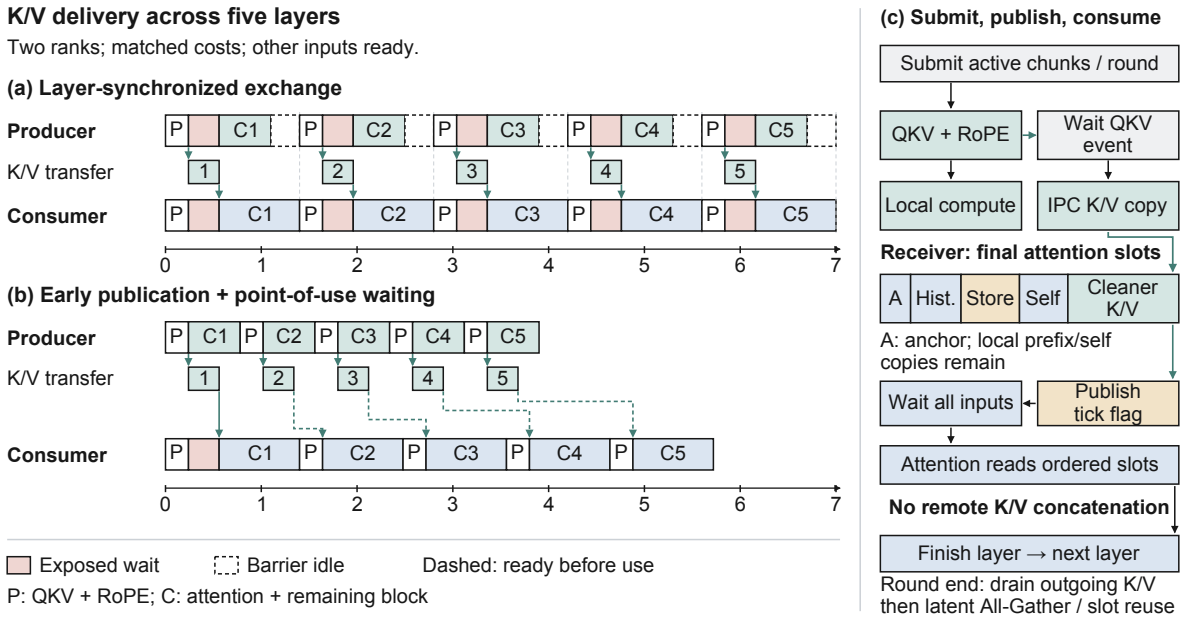


Figure 3: Hiding K/V delivery with identical schematic operation costs. (a) Layer barriers expose communication. (b) Early publication hides later waits, not dependencies or the initial wait. (c) Direct writes to receiver slots precede readiness signals and consumption.

Here N_C is tokens per chunk and N_{prefix} covers anchor, history, and store. Cleaner ranks read fewer keys, permitting later-layer producer lead. WaveRT publishes K/V after QKV projection and RoPE, then checks readiness immediately before attention (Fig. 3).

On a common time base, edge e has payload-ready time t_e^{ready}, consumer local-ready time t_e^{need} before remote waits, and delivery cost τ_e including queueing, transfer, and signaling:

$$\Delta_e = t_e^{\text{need}} - t_e^{\text{ready}}, \qquad w_e = \max(0, \tau_e - \Delta_e). \tag{11}$$

A consumer's exposed wait is the maximum w_e over required inputs. Thus, delivery is fully hidden only when every $\tau_e \le \Delta_e$ (Appendix B.7).

Following software-pipeline principles (NVIDIA, 2026a), *paged* delivery writes K/V directly into ordered attention slots and signals readiness before use, avoiding remote concatenation. When weights, noise draws, positions, and local operators are held fixed, attention consumes the same K/V values as in synchronized execution (Appendix B.6). Appendix B details buffer lifetimes and readiness signaling.

4.3 Local computation and streaming decode

Local computation and K/V delivery require joint optimization. SageAttention (Zhang et al., 2025) and W8A8 target faster local operators but alter producer–consumer progress. K/V quantization reduces payloads, and paged writes reduce receiver-side context assembly. The goal is K/V readiness before each layer's attention, reducing exposed communication and synchronization waits.

Asynchronous decoding overlaps VAE and DiT, but the slower pipeline limits E2E throughput. We use profiled streaming times to balance contiguous VAE partitions across dedicated GPUs while preserving request-local causal caches (Fig. 4). Decoding and inter-stage transfers must sustain DiT's output rate. The first decoded output still incurs pipeline fill latency (Appendix B.5).

WP uses full-model replicas, with execution width determined by the denoising-step count. Logical K/V fan-out remains quadratic in the number of stages, while attention workloads vary across stages. Appendices B.8 and B.4 quantify communication traffic and pipeline fill/drain costs, respectively.

5 Experiments

Table notation. In all experimental tables, teal marks the best value for each metric within its comparison group, and coral marks unusable outcomes.

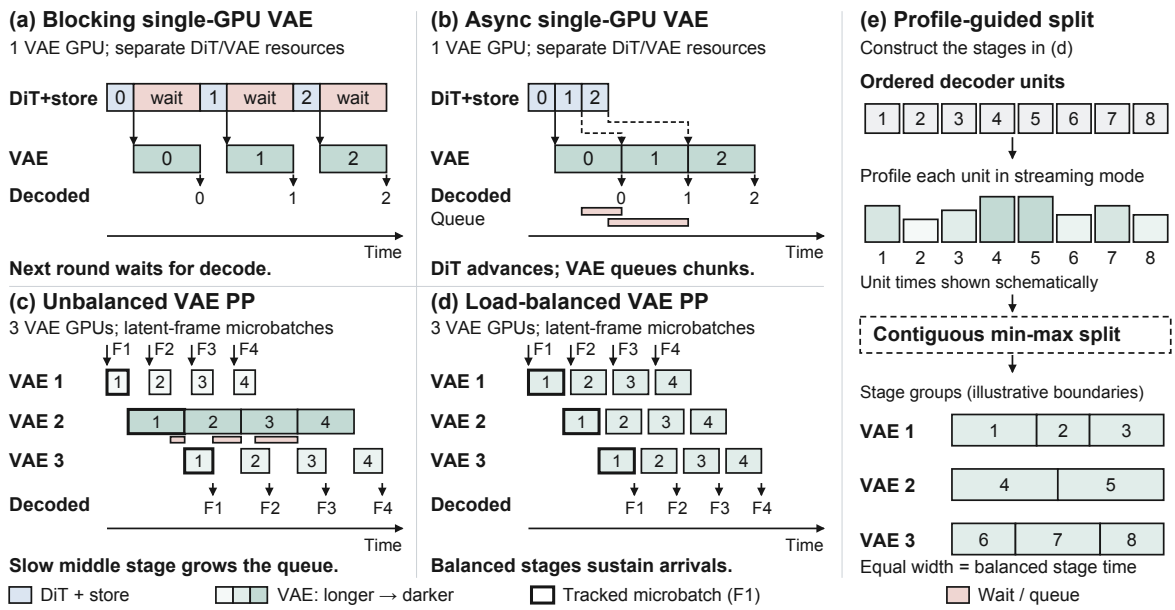


Figure 4: Streaming VAE schedules. Panels (a,b) compare blocking and asynchronous decoding with matched costs. Panels (c,d) compare unbalanced and load-balanced PP under identical workloads and arrivals, with darker teal indicating longer stage service times. Panel (e) shows profile-guided contiguous decoder partitions. Each comparison pair uses its own schematic time scale, with transfers omitted and partition boundaries shown schematically. The first output incurs pipeline fill latency (Appendix B.5).

Models and training. We evaluate 4-step and 5-step Wave Forcing built on Wan2.1-T2V-1.3B (Wan et al., 2025) against Rolling Forcing (Liu et al., 2026) and Causal Forcing (Zhu et al., 2026b). All methods retain their native denoising schedules and three latent frames per chunk. Training and checkpoint details appear in Sec. 3.2 and Appendices A and C.

Evaluation. For short videos, we report VBench (Huang et al., 2024) Total, Quality, Semantic, and Dynamic Degree, generating one 129-frame video per original prompt. For long videos, we report VBench-Long Quality and Dynamic Degree on 200 MovieGen (Polyak et al., 2024) prompts, generating 100-second videos. All videos use 832 × 480 resolution, 16 FPS, and seed 42, and benchmark scores follow official normalization and weighting. Tab. 1 summarizes the results, with the full protocol in Appendix C.

Long-video stability diagnostics. High motion scores can coexist with subject exit or unidirectional camera drift. We assess these failures on a fixed 100-prompt, subject-focused MovieGen subset shared across methods and training ablations. Subject Preservation measures visibility of the SAM3-tracked (Carion et al., 2026) principal entity, with boundary weighting for partial disappearance. Camera Drift penalizes a subject's approach to a frame boundary only with persistent outward background motion in the same direction. Appendix C details prompt selection and both metrics.

Compute configurations. Execution tests use BF16 with FlashAttention-3 (FA3) (Shah et al., 2024) as reference. Sage uses SageAttention (Zhang et al., 2025) with BF16 linear layers, while Sage+W8A8 adds 8-bit linear weights and activations. Both Sage tiers use FA3 cross-attention. These labels describe local computation, not K/V transport precision.

5.1 Generation quality and motion

Tab. 1 compares short- and long-video generation.

We compare open-source models of similar scale. Rolling Forcing (Liu et al., 2026) is evaluated with its original rolling window and with a causal mask under WaveRT. For Causal Forcing (Zhu et al., 2026b), we use the full-attention long-video variant with causal ODE initialization from an autoregressive teacher.

Wave Forcing achieves the best overall balance of quality, motion, and stability (Tab. 1). The 5-step model leads VBench Total (81.64) and Quality (84.40), with VBench-Long Quality of 81.26.

Causal Forcing attains the highest VBench-Long Quality (82.15) and Dynamic Degree (96.61), but its

Table 1: Short- and long-video comparison. Dynamic is Dynamic Degree. Subj./Drift are Subject Preservation/Camera Drift (scores: 0–100). The two FPS columns report DiT-only and end-to-end (E2E) runs.

			Standard VBench ↑				VBench-Long ↑		Stability		FPS ↑	
Method	Steps	GPUs	Total	Quality	Semantic	Dynamic	Quality	Dynamic	Subj. ↑	Drift ↓	DiT	E2E
Rolling Forcing	5	1	81.15	83.77	70.66	51.39	81.18	36.63	92.75	**0.17**	29.12	17.46
+ Causal Attention	5	8	80.89	83.35	**71.05**	37.50	80.50	46.60	91.26	0.40	104.85	96.56
Causal Forcing (Full Attn.)	4	1	79.61	82.83	66.72	**100.00**	**82.15**	**96.61**	71.11	11.14	33.88	19.06
Wave Forcing (Ours)	4	8	80.74	83.93	67.95	84.72	80.89	74.97	91.88	0.36	147.58	**134.81**
+ SageAttention		8	81.03	84.02	69.07	65.28	81.16	77.24	90.79	0.36	**147.78**	134.79
Wave Forcing (Ours)	5	8	**81.64**	**84.40**	70.59	94.44	81.26	91.45	**97.10**	0.37	104.82	96.46
+ SageAttention		8	81.02	83.92	69.41	80.56	81.14	91.14	94.43	0.37	104.80	96.48

Subject Preservation (71.11) and Camera Drift (11.14) indicate unusable stability. The subject disappears at 30 and 75 seconds, leaving pillows and the headboard in view (Fig. 5). Its high motion score accompanies severe subject loss and camera drift.

Rolling Forcing keeps the subject visible (92.75) with the lowest Camera Drift (0.17), but its VBench-Long Dynamic Degree is only 36.63. Wave Forcing raises Dynamic Degree to 91.45 and Subject Preservation to 97.10 while keeping Camera Drift low at 0.37. Its sampled frames retain the reader while showing changes in pose and interaction with the book (Fig. 5). Wave Forcing combines strong motion, visual quality, and stability without an unusable score on any metric.



Figure 5: Qualitative comparison. Rows show Causal Forcing, Rolling Forcing, and 4-step and 5-step Wave Forcing.

5.2 Training ablations

Table 2 reports 4-step training ablations for off-policy DMD and each Stage 3 branch.

Off-policy DMD. Skipping Stage 2 and proceeding directly to on-policy adaptation in Stage 3 reduces Quality from 80.89 to 76.68 and Dynamic Degree from 74.97 to 15.73. Subject Preservation also falls to 76.53, and the principal subject moves out of view (Fig. 6). Off-policy DMD prepares the model to preserve both visual quality and motion during causal adaptation.

Table 2: 4-step training ablations on long videos. All rows evaluate final models. Quality/Dynamic are VBench-Long scores.

Model	Quality ↑	Dynamic ↑	Subj. ↑	Drift ↓
w/o off-policy DMD	76.68	15.73	76.53	0.26
w/o RF	80.19	**88.82**	77.48	6.24
w/o WF	80.34	48.12	**95.64**	**0.10**
w/o SF	75.35	23.66	84.04	1.89
Ours full	**80.89**	74.97	91.88	0.36

Mixed Training Strategy. Removing SF reduces Quality to 75.35 and Dynamic Degree to 23.66, with visible degradation and subject loss (Fig. 6). Removing RF increases Dynamic Degree to 88.82, but Subject Preservation falls to 77.48 and Camera Drift rises to 6.24, the higher motion score reflects unstable framing and subject loss. Removing WF yields the highest Subject Preservation (95.64) and lowest Camera Drift (0.10), but lowers Dynamic Degree to 48.12.

The full model provides the best overall balance, combining the highest Quality (80.89) with strong

Dynamic Degree (74.97), high Subject Preservation (91.88), and low Camera Drift (0.36). It sustains motion and subject stability without an unusable score on any metric. We therefore retain all three branches in the final training recipe.

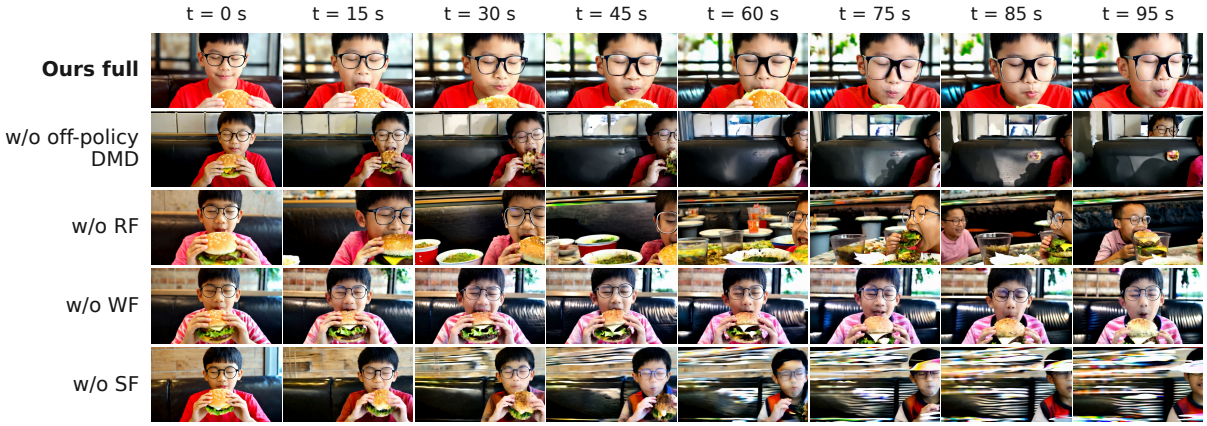


Figure 6: Qualitative training ablations. We compare the full 4-step model with each training ablation.

5.3 End-to-end inference efficiency

We measure 4-step WaveRT at the resolution of 832 × 480 on a single 8×H200 141-GB node, allocating four GPUs to denoising, one to store, and three to VAE decoding. These runs use randomly initialized (dummy) DiT weights, since the corresponding pretrained weights are unavailable and we lack sufficient compute resources to adequately train models at the 14B scale. We report FPS as 1593 decoded frames divided by the median elapsed time over three runs and compute tick p50 from pooled steady-state ticks. DiT timing covers diffusion, communication, store, and pipeline fill/drain, while E2E timing extends through VAE completion. Because VAE decoding overlaps DiT execution, the per-run gap between these timings measures the exposed decoding tail. Loading and file encoding are excluded (Appendix C.3).

Fig. 7a compares runtime and compute configurations. At 1.3B, WaveRT improves BF16 E2E throughput from 127.06 FPS with Sync to 134.81 FPS (6.1%) on the same WF graph. WaveRT + Sage reaches 134.79 E2E FPS versus 147.78 DiT FPS in the same runs (Tab. 4), essentially matching BF16 E2E throughput. Adding W8A8 lowers tick p50 but reduces E2E throughput to 132.89 FPS. At 14B, the corresponding E2E rates are 25.47, 28.64, 28.62, and 33.50 FPS, versus a 5.51-FPS single-GPU reference. Sage alone is again nearly unchanged, whereas Sage+W8A8 is 17.0% faster than BF16. The best single-GPU-relative gains (7.07× at 1.3B and 6.08× at 14B) combine changes to parallelism, the graph, kernels, and decoding.

5.4 System ablations

Fig. 7b fixes the model, WF graph, schedule, topology, and local compute per group, normalizing tick p50 to Sync. Sync gathers layer K/V before attention, whereas Overlap publishes it early. One-sided uses CUDA IPC P2P, Staggered prefetches readiness checks, and Paged writes directly into final attention-buffer slots.

Paged has the lowest tick p50 in all six groups. Sync-to-Paged lowers BF16 tick p50 from 91.96 to 78.88 ms (14.2%) at 1.3B and from 464.27 to 413.80 ms (10.9%) at 14B. The largest adjacent reduction depends on the group, while at 14B BF16 it is Overlap-to-One-sided. Appendix C.3 gives repeat ranges and diagnostics. VAE profiles give 73.15/60.91/80.89 ms, excluding transfers and queueing (Tab. 8).

5.5 Comparison with traditional context parallelism

Fig. 7c,d compares BF16 DiT throughput for attention-level CP (Ulysses and Ring) (Jacobs et al., 2023; Liu et al., 2024) and WP's chunk–stage parallelism across six scales. All methods use 5 steps/6 GPUs for 1.3B–9B and 4 steps/5 GPUs for 14B, satisfying Ulysses' head-divisibility requirement. WP assigns one GPU per denoising stage plus store. Using the architectures listed in Tab. 11, we measure throughput with dummy weights and VAE disabled. We report the mean per-run FPS, including communication and synchronization. Repetition details are given in Appendix D.2.

In the BF16 results, WP leads at five of six scales, with WP/CP ratios of 0.985–1.862×. At 1.3B, WP reaches 150.09 FPS versus 80.60 for Ulysses and 41.19 for Ring. At 9B, WP's 45.70 FPS trails Ulysses' 46.41 by

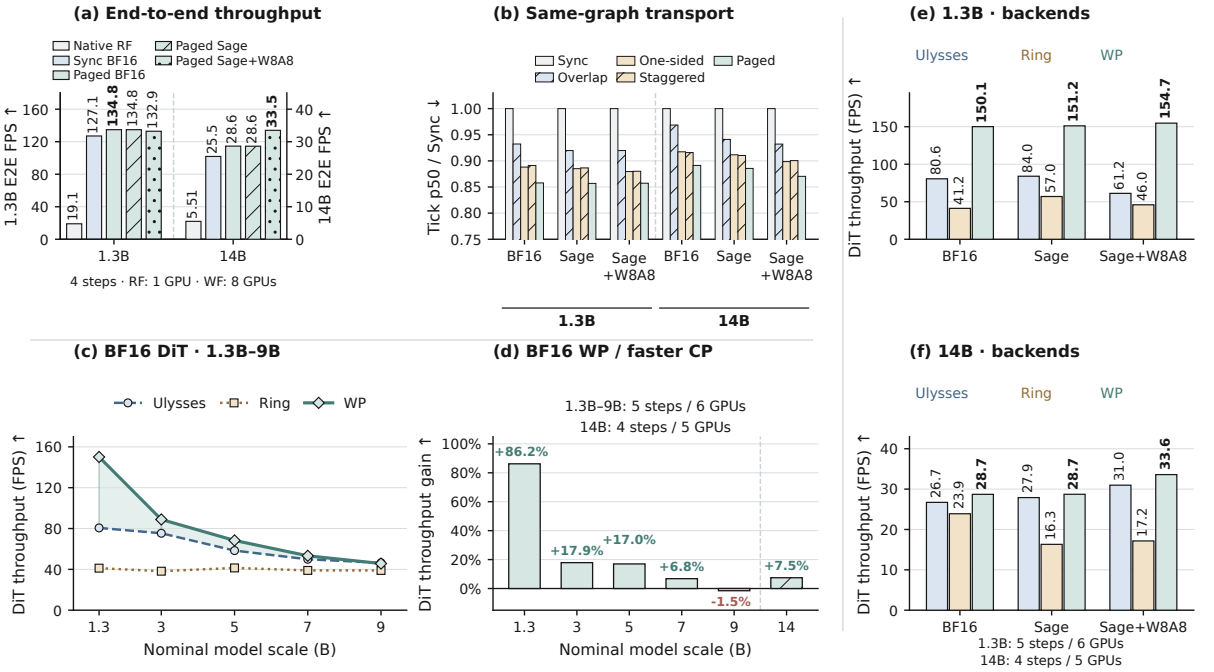


Figure 7: System efficiency with dummy DiT weights. (a) E2E throughput of 4-step WaveRT (8 GPUs) and the single-GPU baseline, with separate axes for 1.3B and 14B. (b) Steady-state tick p50 on the same WF graph, normalized to Sync. (c,d) BF16 DiT throughput across scales and WP's percentage gain over the faster CP baseline. (e,f) DiT throughput across compute backends at 1.3B and 14B. Panels (c–f) disable VAE and use 5 steps/6 GPUs for 1.3B–9B and 4 steps/5 GPUs for 14B. Full measurements and repetition details appear in Tabs. 4 and 6.

1.53%. At 14B, WP reaches 28.71 versus 26.72 FPS for the faster CP. Different step counts, GPU budgets, and VAE concurrency preclude attributing cross-panel FPS differences solely to decoding.

Fig. 7e,f compares backends at 1.3B and 14B, with results for all six scales reported in Tab. 6. The three-run Sage+W8A8 measurements put WP first at every scale (1.025–2.530× the faster CP). These results show that WP's Sage-only advantage varies across scales.

6 Related Work

Efficient streaming video generation. Self Forcing (Huang et al., 2025a) reduces exposure bias by training autoregressive video diffusion on self-generated histories. SGF (Zhuang et al., 2026) restores gradient supervision for historical K/V through two-pass replay, while SGF+ (Su et al., 2026b) separates context-writing and denoising parameters to reduce gradient conflict. Other approaches include few-step causal distillation (Yin et al., 2025; Zhu et al., 2026b) and mixed-noise denoising (Liu et al., 2026). AnyFlow (Gu et al., 2026) learns two-time flow maps with on-policy distillation for variable sampling budgets; Mask Forcing (Zhao et al., 2026b) perturbs DMD self-rollouts with dual-noise masking to improve teacher-mode coverage. For long-horizon streaming, Helios (Yuan et al., 2026) compresses historical and noisy context and simulates drifting during training. Vidu S1 (Zhang et al., 2026c) uses stage-aware noisy and clean history caches for real-time, voice-controlled character generation. Vidu S2 (Zhang et al., 2026b) introduces Self-Replay Forcing and supports dynamic references and streaming editing. These methods motivate studying training objectives together with the context available during streaming inference.

Multi-chunk generation. Blockwise diffusion also appears in language modeling and action generation. D2F (Wang et al., 2025) conditions language generation on partially denoised predecessors, while MBD-LMs (Jin et al., 2026) align training with concurrent decoding of a bounded set of blocks at heterogeneous noise levels. In vision-language-action models, BlockVLA (Wang et al., 2026c) adapts pretrained autoregressive models through block diffusion finetuning, and TBD-VLA (Lee et al., 2026) organizes actions into temporal blocks and supports asynchronous chunk execution through temporal inpainting. Multimodal Diffusion Forcing (Huang et al., 2025c) assigns noise levels across time and modalities to model dependencies within multimodal robot trajectories. These approaches illustrate different choices

of block dependencies; WF specifically trains video chunks to consume cleaner intermediate context through a directed causal wavefront.

Parallel execution. Ulysses (Jacobs et al., 2023) and Ring (Liu et al., 2024) partition individual forward passes, using all-to-all exchange and K/V circulation, respectively. Live Avatar and HiAR (Huang et al., 2025b; Zou et al., 2026) explore pipelined execution with fixed-timestep or matched-noise designs. WP instead schedules chunk–stage tasks on full-model replicas (Sec. 5.5), adapting wavefront scheduling (Hou et al., 2018; Jin et al., 2016) alongside optimized attention and runtimes (Dao et al., 2022; Dao, 2024; Zhang et al., 2025; Zheng et al., 2024).

Video evaluation. VBench (Huang et al., 2024) provides standardized quality, semantic, and motion measures. Our long-video comparisons (Sec. 5.1) show that high Quality and Dynamic Degree can coexist with subject loss and camera drift. We therefore supplement benchmark scores with targeted stability diagnostics; their scope and future alternatives are discussed in Secs. 7 and 8.

These lines frame WF's joint design of causal conditioning, training, and execution, together with the evidence used to assess it. Section 7 examines the remaining methodological and system limits; Sec. 8 connects them to better evaluation, interactive generation, and world modeling.

7 Limitations

Our evaluation establishes streaming generation under fixed conditioning and the tested model, sampling, and hardware configurations. The following limits of the training and execution design discussed in Sec. 6 motivate the agenda in Sec. 8.

Quality evaluation and diagnostic coverage. VBench-based scores do not fully characterize long-stream quality: in our comparisons, high Quality and Dynamic Degree coexist with subject disappearance and camera drift (Sec. 5.1). Subject Preservation and Camera Drift expose these failures, but rely on a 100-prompt subject-focused subset, tracking and identity association, and geometric heuristics (Appendix C.1). Their sensitivity to thresholds and missing observations, coverage of intentional scene changes, and agreement with human judgments remain to be established. They provide targeted diagnostics, with broader perceptual and semantic quality still requiring assessment.

Output-path capacity and attribution. VAE pipelining overlaps and partitions decoding but does not remove its finite service capacity. The 1.3B BF16 configurations reach 147.58/134.81 DiT/E2E FPS at four steps and 104.82/96.46 at five steps (Tab. 1), with three and two VAE GPUs under the eight-GPU budget, respectively. These gaps are consistent with residual decoder/output-path limits. Aggregate timings, however, do not isolate VAE compute, transfers, queueing, or backpressure, and system DiT timing may reflect decoder interference. For 14B BF16, the gap narrows to 28.74 versus 28.64 DiT/E2E FPS (Tab. 4). Matched VAE-on/off runs and stage-level measurements are needed to identify bottlenecks and guide end-to-end resource allocation.

Training complexity. WF currently uses a complex multi-stage training procedure. An important direction is to simplify this procedure while preserving generation quality and long-video stability.

Scalability at a fixed sampling budget. For S DiT denoising steps, WP uses S denoising stages and one cache-refresh stage, each with a full-model replica. Stage parallelism is therefore bounded at a fixed step count, limiting the scale of a single pipeline. Our experiments also show that WP's throughput advantage over CP narrows for larger models. These constraints motivate studying finer-grained or hybrid parallelism and resource sharing across streams.

Interaction and serving scope. High steady-state throughput alone does not establish low input-to-visible-output latency. Online condition changes require deciding when inputs take effect in active chunks and how cached state is refreshed; the fixed-context equivalence argument in Appendix B.6 does not cover these updates. Prompt switching, camera/action control, closed-loop tasks, and multi-stream deadline guarantees require dedicated evaluation beyond the present fixed-conditioning experiments.

8 Future Work

The limits in Sec. 7 define our research agenda: strengthen end-to-end streaming execution, enable online interaction, and then extend toward interactive world models. Serving research and richer quality evaluation support these capability extensions throughout. Appendix E develops the task-specific questions.

End-to-end execution and scalability. We plan to profile decoder stages, transfers, queues, and back-pressure to guide DiT/VAE resource allocation. To address WP's fixed-step scaling limit, we will study finer-grained execution and combinations with context parallelism, checking communication costs and causal dependencies under each design. Simplifying WF's training recipe while preserving motion and long-horizon stability remains a parallel objective.

Serving concurrent streams. StreamDiffusion's image-stream batching (Kodaira et al., 2025) and StreamDiffusionV2's video-stream scheduling (Feng et al., 2026) motivate latency-aware batching. SlackServe (Xia et al., 2026) uses playout slack for resource and quality decisions, while PhysisServe (Physis AI Infra Team, 2026) explores fine-grained stage pipelining. Building on these directions, we aim to study admission control, batching, and resource allocation for concurrent WF streams while respecting their context dependencies. Evaluation should include startup delay, output jitter, playback stalls, fairness, and quality alongside throughput.

Interactive streaming generation. The next capability is updating prompts during generation. LongLive's KV recaching (Yang et al., 2026) provides a starting point for coordinating new conditions with visual history. Extending WF requires defining which active chunks receive each update, refreshing affected state, and adapting training to condition changes. We will assess prompt-to-visible-output latency, prompt adherence, and visual continuity, rather than inferring responsiveness from output FPS.

Interactive world models. Camera and action inputs further introduce feedback-dependent state evolution. We aim to explore both learned world prediction (Zhao et al., 2026a; Su et al., 2026a) and systems in which code or an engine maintains world state while a video model renders observations (Chen et al., 2026; Zhang et al., 2026a). The latter motivates adapting WF for structure-conditioned streaming rendering. Both routes require training under the corresponding control interface and evaluating control alignment, state consistency, and closed-loop behavior. They build on the execution and interaction work above and remain prospective extensions of WF.

Richer quality evaluation. To address the metric limits above, we plan to incorporate streaming-interaction benchmarks such as StreamEval (StreamEval Team, 2026), which evaluates task execution and state consistency under timed inputs alongside visual quality. Long-video understanding methods such as StreamMeCo (Wang et al., 2026a) could help organize temporal evidence for an auxiliary quality judge. We aim to combine automatic diagnostics, understanding-based judgments, and human assessment, with explicit criteria for subject continuity, intended motion, and instruction execution. Such judges require timestamped evidence, calibration against human annotations, and checks for missed failures before their scores can support model comparisons.

9 Conclusion

We present Wave Forcing, which jointly designs causal context, training strategies, and multi-GPU pipelining to denoise multiple video chunks concurrently. WF uses cleaner intermediate states of preceding chunks as context for subsequent chunks, with three-stage training adapting the model to mixed-noise contexts and self-generated histories. A pipeline of full-model replicas then produces one video chunk per concurrent forward round after fill, while WaveRT overlaps K/V delivery with computation to reduce dependency waits. Experiments show that WF improves motion while maintaining overall generation quality and achieves high-throughput streaming video generation. These results demonstrate that jointly designing generation context, training, and execution can translate cross-chunk parallelism into practical gains in video generation efficiency.

Author Contributions

Core idea: Yijie Jin

Feasibility exploration: Yijie Jin*, Jiajun Xu*

Training methods & infrastructure optimization: Yuxuan Liu, Yijie Jin, Ye Huang

Inference implementation & infrastructure optimization: Yijie Jin*, Jiajun Xu*, Jiayang Li, Chenling Hong

Experiments: Yuxuan Liu*, Jiajun Xu*, Yijie Jin, Chuzhi Wang, Ye Huang

Paper Writing: Yijie Jin*, Yuxuan Liu*, Jiajun Xu, Ruiyang Chen

Technical consultation: Xu Wang, Ye Huang

Project leadership: Zhijie Deng

* *Equal contribution within the corresponding category.*

AI Use Statement

AI assistants were used to support conceptual framing and manuscript organization, discuss methodology and systems analogies, interpret available implementation and experimental evidence, translate and edit text, and develop and revise figures. This assistance does not constitute independent verification of the reported results. The authors remain responsible for the paper's claims, citations, and disclosures.

References

Nicolas Carion, Laura Gustafson, Yuan-Ting Hu, Shoubhik Debnath, Ronghang Hu, Didac Suris Coll-Vinent, Chaitanya Ryali, Kalyan Vasudev Alwala, Haitham Khedr, Andrew Huang, Jie Lei, Tengyu Ma, Baishan Guo, Arpit Kalla, Markus Marks, Joseph Greer, Meng Wang, Peize Sun, Roman Rädle, Triantafyllos Afouras, Effrosyni Mavroudi, Katherine Xu, Tsung-Han Wu, Yu Zhou, Liliane Momeni, Rishi Hazra, Shuangrui Ding, Sagar Vaze, Francois Porcher, Feng Li, Siyuan Li, Aishwarya Kamath, Ho Kei Cheng, Piotr Dollar, Nikhila Ravi, Kate Saenko, Pengchuan Zhang, and Christoph Feichtenhofer. SAM 3: Segment anything with concepts. In *International Conference on Learning Representations*, pages 138846–138923, 2026. URL https://proceedings.iclr.cc/paper_files/paper/2026/hash/e0982cbc81401df3430ee1ff780dc7a2-Abstract-Conference.html.

Mathilde Caron, Hugo Touvron, Ishan Misra, Hervé Jégou, Julien Mairal, Piotr Bojanowski, and Armand Joulin. Emerging properties in self-supervised vision transformers. In *IEEE/CVF International Conference on Computer Vision*, pages 9630–9640. IEEE, 2021.

Yiwen Chen, Guosheng Lin, and Chi Zhang. Code World Model: Coding agent as world brain. *arXiv preprint arXiv:2608.25927*, 2026. URL https://arxiv.org/abs/2608.25927.

Tri Dao. FlashAttention-2: Faster attention with better parallelism and work partitioning. In *International Conference on Learning Representations*, pages 35549–35562, 2024. URL https://proceedings.iclr.cc/paper_files/paper/2024/hash/98ed250b203d1ac6b24bbcf263e3d4a7-Abstract-Conference.html.

Tri Dao, Daniel Y. Fu, Stefano Ermon, Atri Rudra, and Christopher Ré. FlashAttention: Fast and memory-efficient exact attention with IO-Awareness. In *Advances in Neural Information Processing Systems*, volume 35, pages 16344–16359, 2022. doi: 10.52202/068431-1189. URL https://proceedings.neurips.cc/paper_files/paper/2022/hash/67d57c32e20fd0a7a302cb81d36e40d5-Abstract.html.

Guian Fang, Shengju Qian, Dongyue Lu, Junchao Huang, Lutao Jiang, Xin Wang, Yiren Song, Li Jiang, and Mike Zheng Shou. SolarRenderer: Few-step generative reference rendering, 2026. URL https://arxiv.org/abs/2610.28630.

Tianrui Feng, Zhi Li, Shuo Yang, Haocheng Xi, Muyang Li, Xiuyu Li, Lvmin Zhang, Keting Yang, Kelly Peng, Song Han, Maneesh Agrawala, Kurt Keutzer, Akio Kodaira, and Chenfeng Xu. StreamDiffusionV2: A streaming system for dynamic and interactive video generation. In *Proceedings of Machine Learning and Systems*, volume 8, 2026. URL https://proceedings.mlsys.org/paper_files/paper/2026/hash/698cfaf72a208aef2e78bcac55b74328-Abstract-Conference.html.

Yuchao Gu, Guian Fang, Yuxin Jiang, Weijia Mao, Song Han, Han Cai, and Mike Zheng Shou. AnyFlow: Any-step video diffusion model with on-policy flow map distillation. In *Computer Vision - ECCV 2026 - 19th European Conference, Malmö, Sweden, September 8-12, 2026, Proceedings, Part LII*, volume 17052 of

Lecture Notes in Computer Science, pages 163–181. Springer, 2026. doi: 10.1007/978-3-032-37235-2_10. URL https://link.springer.com/chapter/10.1007/978-3-032-37235-2_10.

Kaixi Hou, Hao Wang, Wu-chun Feng, Jeffrey S. Vetter, and Seyong Lee. Highly efficient compensation-based parallelism for wavefront loops on GPUs. In *IEEE International Parallel and Distributed Processing Symposium*, pages 276–285. IEEE, 2018.

Junchao Huang, Guian Fang, Shengju Qian, Xianghao Kong, Zhuoran Zhao, Wei Huang, Yihua Du, Zixin Zhang, Justin Cui, Yuchao Gu, Yukang Chen, Xinting Hu, Tianyu He, Shaoshuai Shi, Zhuotao Tian, Xin Wang, Mike Zheng Shou, and Li Jiang. SolarWM: Open data and scalable training for long-horizon video world models, 2026a. URL https://arxiv.org/abs/2609.02886.

Xun Huang, Zhengqi Li, Guande He, Mingyuan Zhou, and Eli Shechtman. Self forcing: Bridging the train-test gap in autoregressive video diffusion. In *Advances in Neural Information Processing Systems*, volume 38, pages 167283–167308, 2025a. doi: 10.52202/085713-5576. URL https://proceedings.neurips.cc/paper_files/paper/2025/hash/f4823f831af67a3ef15e41a85434422a-Abstract-Conference.html.

Yubo Huang, Hailong Guo, Fangtai Wu, Weiqiang Wang, Shifeng Zhang, Shijie Huang, Qijun Gan, Lin Liu, Sirui Zhao, Enhong Chen, Jiaming Liu, and Steven Hoi. Live avatar: Streaming real-time audio-driven avatar generation with infinite length. *arXiv preprint arXiv:2512.04677*, 2025b. URL https://arxiv.org/abs/2512.04677.

Ziqi Huang, Yinan He, Jiashuo Yu, Fan Zhang, Chenyang Si, Yuming Jiang, Yuanhan Zhang, Tianxing Wu, Qingyang Jin, Nattapol Chanpaisit, Yaohui Wang, Xinyuan Chen, Limin Wang, Dahua Lin, Yu Qiao, and Ziwei Liu. VBench: Comprehensive benchmark suite for video generative models. In *Proceedings of the IEEE/CVF Conference on Computer Vision and Pattern Recognition*, pages 21807–21818. IEEE, 2024. URL https://github.com/Vchitect/VBench.

Ziqi Huang, Fan Zhang, Xiaojie Xu, Yinan He, Jiashuo Yu, Ziyue Dong, Qianli Ma, Nattapol Chanpaisit, Chenyang Si, Yuming Jiang, Yaohui Wang, Xinyuan Chen, Ying-Cong Chen, Limin Wang, Dahua Lin, Yu Qiao, and Ziwei Liu. VBench++: Comprehensive and versatile benchmark suite for video generative models. *IEEE Transactions on Pattern Analysis and Machine Intelligence*, 48(3):3268–3285, 2026b. doi: 10.1109/TPAMI.2025.3633890.

Zixuan Huang, Huaidian Hou, and Dmitry Berenson. Multimodal diffusion forcing for forceful manipulation. *arXiv preprint arXiv:2511.04812*, 2025c. URL https://arxiv.org/abs/2511.04812.

Sam Ade Jacobs, Masahiro Tanaka, Chengming Zhang, Minjia Zhang, Shuaiwen Leon Song, Samyam Rajbhandari, and Yuxiong He. DeepSpeed Ulysses: System optimizations for enabling training of extreme long sequence transformer models. *arXiv preprint arXiv:2309.14509*, 2023. URL https://arxiv.org/abs/2309.14509.

Tian Jin, Nirmal Prajapati, Waruna Ranasinghe, Guillaume Iooss, Yun Zou, Sanjay Rajopadhye, and David Wonnacott. Hybrid static/dynamic schedules for tiled polyhedral programs. *arXiv preprint arXiv:1610.07236*, 2016. URL https://arxiv.org/abs/1610.07236.

Yijie Jin, Jiajun Xu, Yuxuan Liu, Chenkai Xu, Yi Tu, Jiajun Li, Dandan Tu, Xiaohui Yan, Kai Yu, Pengfei Liu, and Zhijie Deng. Multi-block diffusion language models. *arXiv preprint arXiv:2606.29215*, 2026. URL https://arxiv.org/abs/2606.29215.

Akio Kodaira, Chenfeng Xu, Toshiki Hazama, Takanori Yoshimoto, Kohei Ohno, Shogo Mitsuhori, Soichi Sugano, Hanying Cho, Zhijian Liu, Masayoshi Tomizuka, and Kurt Keutzer. StreamDiffusion: A pipeline-level solution for real-time interactive generation. In *Proceedings of the IEEE/CVF International Conference on Computer Vision*, pages 12371–12380, 2025. URL https://openaccess.thecvf.com/content/ICCV2025/papers/Kodaira_StreamDiffusion_A_Pipeline-level_Solution_for_Real-Time_Interactive_Generation_ICCV_2025_paper.pdf.

Sung-Wook Lee, Xuhui Kang, and Yen-Ling Kuo. TBD-VLA: Temporal block diffusion vision language action model. *arXiv preprint arXiv:2606.07895*, 2026. URL https://arxiv.org/abs/2606.07895.

Xinye Li, Lingshuai Lin, Lei Wang, Liuzhou Zhang, Jialin Cui, Qingshan Li, Guanchu Wang, Qingbin Liu, Xi Chen, Jiang Bian, and Wai Lam. ForgeWM: Progressive causal training for few-step action-conditioned video world models. *arXiv preprint arXiv:2608.14022*, 2026. URL https://arxiv.org/abs/2608.14022.

Hao Liu, Matei Zaharia, and Pieter Abbeel. RingAttention with blockwise transformers for near-infinite context. In *International Conference on Learning Representations*, pages 3992–4008, 2024. URL https://proceedings.iclr.cc/paper_files/paper/2024/hash/1119587863e78451f080da2a768c4935-Abstract-Conference.html.

Kunhao Liu, Wenbo Hu, Jiale Xu, Ying Shan, and Shijian Lu. Rolling forcing: Autoregressive long video diffusion in real time. In *International Conference on Learning Representations*, pages 91177–91196, 2026. URL https://proceedings.iclr.cc/paper_files/paper/2026/hash/935151cc6cb5d8b6816133b75233775a-Abstract-Conference.html.

Yanzuo Lu, Tian Ye, Yitong Li, Shuchen Xue, Haozhe Liu, Song Han, and Enze Xie. StreamRender-H3: Interactive coding worlds with real-time streaming diffusion render. Research blog, 2026. URL https://nvlabs.github.io/Sana/Sol-Engine/StreamRender-H3/.

NVIDIA. *NVIDIA Ampere GPU Architecture Tuning Guide*, 2026a. URL https://docs.nvidia.com/cuda/ampere-tuning-guide/index.html. CUDA 13.4, Secs. 1.4.1.2–1.4.1.3. Accessed September 21, 2026.

NVIDIA. *CUTLASS: Efficient GEMM in CUDA*, 2026b. URL https://docs.nvidia.com/cutlass/latest/media/docs/cpp/efficient_gemm.html. Software Pipelining section. Accessed September 21, 2026.

Physis AI Infra Team. PhysisServe: Efficient autoregressive denoising serving with fine-grained stage-wise pipelining. Technical blog, October 2026. URL https://physis-ai.com/blog/physisserve/en.

Adam Polyak, Amit Zohar, Andrew Brown, Andros Tjandra, Animesh Sinha, Ann Lee, Apoorv Vyas, Bowen Shi, Chih-Yao Ma, Ching-Yao Chuang, David Yan, Dhruv Choudhary, Dingkang Wang, Geet Sethi, Guan Pang, Haoyu Ma, Ishan Misra, Ji Hou, Jialiang Wang, Kiran Jagadeesh, Kunpeng Li, Luxin Zhang, Mannat Singh, Mary Williamson, Matt Le, Matthew Yu, Mitesh Kumar Singh, Peizhao Zhang, Peter Vajda, Quentin Duval, Rohit Girdhar, Roshan Sumbaly, Sai Saketh Rambhatla, Sam Tsai, Samaneh Azadi, Samyak Datta, Sanyuan Chen, Sean Bell, Sharadh Ramaswamy, Shelly Sheynin, Siddharth Bhattacharya, Simran Motwani, Tao Xu, Tianhe Li, Tingbo Hou, Wei-Ning Hsu, Xi Yin, Xiaoliang Dai, Yaniv Taigman, Yaqiao Luo, Yen-Cheng Liu, Yi-Chiao Wu, Yue Zhao, Yuval Kirstain, Zecheng He, Zijian He, Albert Pumarola, Ali Thabet, Artsiom Sanakoyeu, Arun Mallya, Baishan Guo, Boris Araya, Breena Kerr, Carleigh Wood, Ce Liu, Cen Peng, Dimitry Vengertsev, Edgar Schonfeld, Elliot Blanchard, Felix Juefei-Xu, Fraylie Nord, Jeff Liang, John Hoffman, Jonas Kohler, Kaolin Fire, Karthik Sivakumar, Lawrence Chen, Licheng Yu, Luya Gao, Markos Georgopoulos, Rashel Moritz, Sara K. Sampson, Shikai Li, Simone Parmeggiani, Steve Fine, Tara Fowler, Vladan Petrovic, and Yuming Du. Movie gen: A cast of media foundation models. *arXiv preprint arXiv:2410.13720*, 2024. URL https://arxiv.org/abs/2410.13720.

Jay Shah, Ganesh Bikshandi, Ying Zhang, Vijay Thakkar, Pradeep Ramani, and Tri Dao. FlashAttention-3: Fast and accurate attention with asynchrony and low-precision. In *Advances in Neural Information Processing Systems*, volume 37, pages 68658–68685, 2024. doi: 10.52202/079017-2193. URL https://proceedings.neurips.cc/paper_files/paper/2024/hash/7ede97c3e082c6df10a8d6103a2eebd2-Abstract-Conference.html.

StreamEval Team. StreamEval: Evaluating interactive streaming video generation models. *arXiv preprint arXiv:2610.28402*, 2026. URL https://arxiv.org/abs/2610.28402.

Yue Su, Bokai Lin, Xinkai Wang, Chubin Zhang, Xiangnan Wu, Kuan Zhang, Weiyang Jin, Jiwen Yu, Yiming Li, Cewu Lu, Lixin Yang, and Xihui Liu. Can world and action modeling benefit each other under unified causal training? *arXiv preprint arXiv:2610.21095*, 2026a. URL https://arxiv.org/abs/2610.21095.

Zihan Su, Junhao Zhuang, Yaowei Li, Siwen Lu, Haoran Li, Lingen Li, Haoyu Wu, Weiyang Jin, Songchun Zhang, Haoyang Huang, Chun Yuan, Zeyue Xue, and Nan Duan. SGF+: Decoupling gradient flows for autoregressive video generation. *arXiv preprint arXiv:2610.10429*, 2026b. URL https://arxiv.org/abs/2610.10429.

Team Wan, Ang Wang, Baole Ai, Bin Wen, Chaojie Mao, Chen-Wei Xie, Di Chen, Feiwu Yu, Haiming Zhao, Jianxiao Yang, Jianyuan Zeng, Jiayu Wang, Jingfeng Zhang, Jingren Zhou, Jinkai Wang, Jixuan Chen, Kai Zhu, Kang Zhao, Keyu Yan, Lianghua Huang, Mengyang Feng, Ningyi Zhang, Pandeng Li, Pingyu Wu, Ruihang Chu, Ruili Feng, Shiwei Zhang, Siyang Sun, Tao Fang, Tianxing Wang, Tianyi Gui, Tingyu Weng, Tong Shen, Wei Lin, Wei Wang, Wei Wang, Wenmeng Zhou, Wente Wang, Wenting Shen, Wenyuan Yu, Xianzhong Shi, Xiaoming Huang, Xin Xu, Yan Kou, Yangyu Lv, Yifei Li, Yijing Liu, Yiming Wang, Yingya Zhang, Yitong Huang, Yong Li, You Wu, Yu Liu, Yulin Pan, Yun Zheng, Yuntao Hong, Yupeng Shi, Yutong Feng, Zeyinzi Jiang, Zhen Han, Zhi-Fan Wu, and Ziyu Liu. Wan:

Open and advanced large-scale video generative models. *arXiv preprint arXiv:2503.20314*, 2025. URL https://arxiv.org/abs/2503.20314.

Junxi Wang, Te Sun, Jiayi Zhu, Junxian Li, Haowen Xu, Zichen Wen, Xuming Hu, Zhiyu Li, and Linfeng Zhang. StreamMeCo: Long-term agent memory compression for efficient streaming video understanding. In *Findings of the Association for Computational Linguistics: ACL 2026*, pages 13234–13251. Association for Computational Linguistics, 2026a. doi: 10.18653/v1/2026.findings-acl.647. URL https://aclanthology.org/2026.findings-acl.647/.

Junxi Wang, Te Sun, Jiayi Zhu, Chen Zhang, Siyuan Li, Xuyang Liu, Zichen Wen, Xiaobing Tu, Jinkui Ren, Xiantao Zhang, Ziqi Yuan, and Linfeng Zhang. MemForest: Efficient agent memory management via EventTree partitioning and progressive merging. *arXiv preprint arXiv:2609.08273*, 2026b. URL https://arxiv.org/abs/2609.08273.

Ruiheng Wang, Shuanghao Bai, Haoran Zhang, Badong Chen, and Xiangyu Xu. BlockVLA: Accelerating autoregressive VLA via block diffusion finetuning. *arXiv preprint arXiv:2605.13382*, 2026c. URL https://arxiv.org/abs/2605.13382.

Xu Wang, Chenkai Xu, Yijie Jin, Jiachun Jin, Hao Zhang, and Zhijie Deng. Diffusion LLMs can do faster-than-AR inference via discrete diffusion forcing. *arXiv preprint arXiv:2508.09192*, 2025. URL https://arxiv.org/abs/2508.09192.

Yifei Xia, Hao Yuan, Suhan Ling, Haoran Sun, Hanke Zhang, Xupeng Miao, Fangcheng Fu, and Bin Cui. Adaptive resource management and quality control for streaming video generation. *arXiv preprint arXiv:2606.15319*, 2026. URL https://arxiv.org/abs/2606.15319.

Shuai Yang, Wei Huang, Ruihang Chu, Yicheng Xiao, Yuyang Zhao, Xianbang Wang, Muyang Li, Enze Xie, Yingcong Chen, Yao Lu, Song Han, and Yukang Chen. LongLive: Real-time interactive long video generation. In *International Conference on Learning Representations*, pages 90037–90059, 2026. URL https://proceedings.iclr.cc/paper_files/paper/2026/hash/91a1610c6ed9e02d33f826b46f472b92-Abstract-Conference.html.

Tianwei Yin, Michaël Gharbi, Richard Zhang, Eli Shechtman, Frédo Durand, William T. Freeman, and Taesung Park. One-step diffusion with distribution matching distillation. In *Proceedings of the IEEE/CVF Conference on Computer Vision and Pattern Recognition*, pages 6613–6623. IEEE, 2024. URL https://openaccess.thecvf.com/content/CVPR2024/html/Yin_One-step_Diffusion_with_Distribution_Matching_Distillation_CVPR_2024_paper.html.

Tianwei Yin, Qiang Zhang, Richard Zhang, William T. Freeman, Fredo Durand, Eli Shechtman, and Xun Huang. From slow bidirectional to fast autoregressive video diffusion models. In *Proceedings of the IEEE/CVF Conference on Computer Vision and Pattern Recognition*, pages 22963–22974. IEEE, 2025. URL https://openaccess.thecvf.com/content/CVPR2025/html/Yin_From_Slow_Bidirectional_to_Fast_Autoregressive_Video_Diffusion_Models_CVPR_2025_paper.html.

Shenghai Yuan, Yuanyang Yin, Zongjian Li, Xinwei Huang, Xiao Yang, and Li Yuan. Helios: Real real-time long video generation model. *arXiv preprint arXiv:2603.04379*, 2026. URL https://arxiv.org/abs/2603.04379.

Ailing Zeng, Casper Yang, Chauncey Ge, Eddie Zhang, Garvey Xu, Gavin Lin, Gilbert Gu, Jeremy Pi, Leo Li, Mingyi Shi, Shawn Wang, Sheng Bi, Steven Tang, Thorn Hang, Tobey Guo, Vincent Li, Xin Tong, Yikang Li, Yuchen Sun, Yue Zhao, Yuhan Lu, Yuwei Li, Zane Zhang, Zeshi Yang, and Zi Ye. LPM 1.0: Video-based character performance model. *arXiv preprint arXiv:2604.07823*, 2026. URL https://arxiv.org/abs/2604.07823.

Jihai Zhang, Runjia Qian, Kaiqin Kong, Biao Jiang, Puyi Wang, Siru Chen, Tianle Li, Guanjie Chen, Junyi Wu, Chubin Chen, Yuanhang Li, Kaichen Huang, Haobo Zhang, Yangguang Li, Wei Yu, Guibin Chen, Yu Cheng, and Yahui Zhou. Matrix-Game 4.0: Harnessing video models for real-time playable game worlds. *arXiv preprint arXiv:2610.27999*, 2026a. URL https://arxiv.org/abs/2610.27999.

Jintao Zhang, Jia Wei, Pengle Zhang, Jun Zhu, and Jianfei Chen. SageAttention: Accurate 8-bit attention for plug-and-play inference acceleration. In *International Conference on Learning Representations*, pages 71566–71585, 2025. URL https://proceedings.iclr.cc/paper_files/paper/2025/hash/b286c344d38e10d2466c0514b78e2f36-Abstract-Conference.html.

Jintao Zhang, Kai Jiang, Jintao Chen, Xu Wang, Deyuan Liu, Jungang Li, Dechuang Chen, Ming Lin, Jingjiang Zhou, Haopeng Jin, Qi Jia, Xiaohang Wang, Yaole Wang, Zhanqiang Zhang, Ran Li, Zhengkun Huang, Shuyue Xiong, Yuji Wang, Zikun Dai, Hui He, Yang Luo, Mang Ning, Weiqi Feng, Chengyang

Ye, Xinyue Lin, Min Zhao, Hongzhou Zhu, Hengkai Tan, Zeyuan Wang, Chendong Xiang, Kaiwen Zheng, Zhijie Deng, Fan Bao, Jianfei Chen, and Jun Zhu. Vidu S2: Real-time interactive, editable, and spatial video generation. *arXiv preprint arXiv:2609.11638*, 2026b. URL https://arxiv.org/abs/2609.11638.

Jintao Zhang, Kai Jiang, Jintao Chen, Xu Wang, Yang Luo, Yuji Wang, Dechuang Chen, Jungang Li, Chengyang Ye, Marco Chen, Hongzhou Zhu, Min Zhao, Yuxuan Jiang, Zhengkun Huang, Chendong Xiang, Kaiwen Zheng, Haoxu Wang, Xiaohang Wang, Qi Jia, Xin Chen, Yimin Chen, Youhe Jiang, Fangcheng Fu, Zhijie Deng, Fan Bao, Jianfei Chen, and Jun Zhu. Vidu S1: A real-time interactive video generation model. *arXiv preprint arXiv:2607.03118*, 2026c. URL https://arxiv.org/abs/2607.03118.

Richard Zhang, Phillip Isola, Alexei A. Efros, Eli Shechtman, and Oliver Wang. The unreasonable effectiveness of deep features as a perceptual metric. In *Proceedings of the IEEE Conference on Computer Vision and Pattern Recognition*, pages 586–595. IEEE, 2018. URL https://openaccess.thecvf.com/content_cvpr_2018/html/Zhang_The_Unreasonable_Effectiveness_CVPR_2018_paper.html.

Min Zhao, Hongzhou Zhu, Bokai Yan, Zihan Zhou, Yimin Chen, Honglie Wang, Wenqiang Sun, Zhengwei Fang, Zizheng Xun, Zihao Li, Kaiwen Zheng, Guande He, Xiao Yang, Chongxuan Li, Fan Bao, and Jun Zhu. minWM: A full-stack open-source framework for real-time interactive video world models. *arXiv preprint arXiv:2605.30263*, 2026a. URL https://arxiv.org/abs/2605.30263.

Zhuoran Zhao, Shengju Qian, Tongtong Liang, Xianghao Kong, Songchun Zhang, Junchao Huang, Guian Fang, Xin Wang, Pan Hui, and Anyi Rao. Mask Forcing: Improving autoregressive video diffusion distillation via dual-noise masking rollout, 2026b. URL https://arxiv.org/abs/2609.09123.

Lianmin Zheng, Liangsheng Yin, Zhiqiang Xie, Chuyue Sun, Jeff Huang, Cody Hao Yu, Shiyi Cao, Christos Kozyrakis, Ion Stoica, Joseph E. Gonzalez, Clark Barrett, and Ying Sheng. SGLang: Efficient execution of structured language model programs. In *Advances in Neural Information Processing Systems*, volume 37, pages 62557–62583, 2024. doi: 10.52202/079017-2000. URL https://proceedings.neurips.cc/paper_files/paper/2024/hash/724be4472168f31ba1c9ac630f15dec8-Abstract-Conference.html.

Yuqian Zhou, Zhenghong Zhou, Zongze Wu, Cameron Smith, Richard Zhang, Jiebo Luo, Eli Shechtman, and Zhe Lin. EditStream: A unified autoregressive framework for interactive video generation and editing. *arXiv preprint arXiv:2608.21424*, 2026. URL https://arxiv.org/abs/2608.21424.

Haoyi Zhu, Haozhe Liu, Yuyang Zhao, Tian Ye, Junsong Chen, Jincheng Yu, Tong He, Song Han, and Enze Xie. SANA-WM: Efficient minute-scale world modeling with hybrid linear diffusion transformer. *arXiv preprint arXiv:2605.15178*, 2026a. URL https://arxiv.org/abs/2605.15178.

Hongzhou Zhu, Min Zhao, Guande He, Hang Su, Chongxuan Li, and Jun Zhu. Causal forcing: Autoregressive diffusion distillation done right for high-quality real-time interactive video generation. *arXiv preprint arXiv:2602.02214*, 2026b. URL https://arxiv.org/abs/2602.02214.

Junhao Zhuang, Shiyi Zhang, Yuxuan Bian, Yaowei Li, Yawen Luo, Yijun Liu, Weiyang Jin, Songchun Zhang, Xianglong He, Xuying Zhang, Haoran Li, Haoyang Huang, Zeyue Xue, and Nan Duan. Self gradient forcing: Native long video extrapolation. *arXiv preprint arXiv:2607.20368*, 2026. URL https://arxiv.org/abs/2607.20368.

Kai Zou, Dian Zheng, Hongbo Liu, Tiankai Hang, Bin Liu, and Nenghai Yu. HiAR: Efficient autoregressive long video generation via hierarchical denoising. In *European Conference on Computer Vision*, pages 225–242. Springer, 2026. URL https://link.springer.com/chapter/10.1007/978-3-032-37026-6_13.

A Training Implementation Details

Noise schedules and score networks. The 4-step schedule is $[1000, 750, 500, 250]$ and the 5-step schedule is $[1000, 800, 600, 400, 200]$, before timestep warping with shift factor 5. Both use three latent frames per chunk and preserve their respective schedules through all stages and inference. The frozen DMD teacher is bidirectional Wan2.1-T2V-14B. The trainable fake-score model starts from bidirectional Wan2.1-T2V-1.3B and does not share weights with the causal student. It learns to denoise noisy, detached student predictions. Stage transitions transfer raw student weights and restart the fake-score model, optimizer, and EMA states. Evaluation uses the resulting EMA student.

Off-policy targets and perceptual loss. Stage 2 uses 2048 training and 128 validation teacher examples generated by Wan2.1-T2V-14B with 50 denoising steps, guidance scale 3, and timestep shift 5. Each example contains 21 latent frames. The off-policy implementation samples S consecutive chunks ($3S$ latent frames), constructs student K/V from preceding clean teacher chunks, and re-noises the sampled chunks to form a set of chunks at staggered noise levels. DMD and LPIPS are applied to the same clean prediction, with LPIPS weight 0.25 for both model versions. The fake-score update uses student predictions from these teacher-derived states.

For LPIPS, latent spatial resolution is bilinearly reduced from 60×104 to 30×52, then decoded by a frozen Wan VAE to 240×416 RGB frames. Every third decoded frame is evaluated. The 4-step training input contains 12 latent frames and decodes to 45 frames, giving 15 perceptual comparisons. The 5-step training input contains 15 latent frames and decodes to 57 frames, giving 19 comparisons. Decoded values are clamped to $[-1, 1]$, and VGG-based LPIPS is averaged over the sampled frames.

Optimization and updates. The student and fake-score learning rates are 1.5×10^{-6} and 4×10^{-7}, with Adam moments $(0, 0.999)$. EMA uses decay 0.99 and starts after 200 training iterations. The training used eight workers with one sample each and no gradient accumulation, giving an effective batch size of eight. For the three-stage 4-step model, the 3000/1000/2000 training-loop iterations correspond to 600/1000/400 student updates and 3000/1000/2000 fake-score updates. The 5-step model starts from released RF weights and proceeds directly to Stage 2 (Sec. 3.2), so the Stage 1 iteration and update counts apply only to the 4-step model. Stage 1 and Stage 3 update the student once per five fake-score updates, whereas Stage 2 updates both models each iteration.

Rollout visibility. The Stage 3 sampler selects RF, WF, or SF for the same student with equal probability. The WF path reuses the RF rollout implementation with chunk-wise causal attention to advance the wavefront: clean history and the same or earlier active chunks are visible, while later active chunks are masked. This matches Eq. (4). The RF and SF paths remain complementary training distributions.

B Runtime Implementation and Analysis

B.1 Process ownership and reference execution

WaveRT uses S denoising processes and one store process, each owning a GPU and a full DiT replica. A dedicated group of P_{VAE} GPUs owns contiguous decoder partitions, giving $S + 1 + P_{\text{VAE}}$ GPUs. GPU allocations list denoising + Store + VAE: $4 + 1 + 3$ for 4-step and $5 + 1 + 2$ for 5-step WaveRT, both totaling eight GPUs. The store process performs a full clean-state cache refresh, rather than an additional denoising update.

The local forward uses SGLang Diffusion for loading, conditioning, scheduling, dense operators, and cross-attention. WaveRT interposes after self-attention QKV projection and RoPE to publish K/V and construct the legal context. It owns the temporal pages and replaces the base runtime's unused large self-attention cache with a placeholder. The execution tests use BF16/FA3 as the reference backend. The approximate compute modes replace self-attention with SageAttention and optionally use W8A8 linear layers, while retaining FA3 for cross-attention.

The synchronized reference gathers every rank's layer K/V, including store:

$$((K^{\ell}_{k,r}, V^{\ell}_{k,r}))^{S}_{r=0} = \text{AllGather}^{S}_{r=0}(K^{\ell}_{k,r}, V^{\ell}_{k,r}). \tag{12}$$

Idle ranks provide dummy payloads during fill/drain, but their slots never enter attention. Each active rank keeps all query heads. The RF path reads every active denoising slot, whereas WF selects the context in Eq. (5). Synchronized and asynchronous WF share the same context rules. Native RF comparison additionally changes the visibility graph and requires matching history and positions.

Algorithm 1 WaveRT round schedule (one request, N_{chunk} chunks)

Require: S denoising ranks, store rank S, identical weights and fixed scheduler
Initialize empty anchor/history and generation-indexed K/V buffers
for $k = 0, \ldots, N_{\text{chunk}} + S - 1$ **do**
  On each rank r, execute the following concurrently with $i = k - r$
  if $r < S$ and $0 \le i < N_{\text{chunk}}$ **then**
    Rank 0 admits $Z_i^{(0)}$, while other ranks use the previous tick's latent
    for $\ell = 1, \ldots, L$ **do**
      Produce local Q/K/V and publish K/V to active ranks $s < r$
      Wait for legal cleaner-rank and store pages for (k, ℓ)
      Apply attention with Eq. (5), then finish the layer
    end for
    Apply the stage transition with noise keyed by chunk and stage
  else if $r = S$ and $0 \le i < N_{\text{chunk}}$ **then**
    Refresh K/V from clean B_i and publish each layer's K/V to active denoising ranks
    Enqueue B_i for the streaming VAE
  end if
  Drain outgoing copies and promote the current store page into history
  All ranks participate in latent All-Gather, after which each receiver takes its predecessor's output
end for

B.2 K/V publication and buffer lifetime

At initialization, consumers allocate remote K/V slots and device-side generation flags indexed by producer, round buffer, and layer, then exchange IPC memory handles. After rank j produces layer ℓ K/V, its communication stream waits on the producer event, copies the payload to each active consumer $s < j$, and publishes the generation flag. A consumer's compute stream waits for the matching flag immediately before attention. All legal cleaner ranks, including nonadjacent chunks and active store, must be ready.

This produce–publish–wait-before-use order follows buffered software-pipeline principles (NVIDIA, 2026a;b), applied here to newly computed inter-GPU K/V rather than prefetched static tiles. Causal visibility permits producer lead but does not guarantee it. WaveRT enforces the order explicitly because ordinary CTA scheduling supplies no such guarantee. The CUDA IPC implementation uses `cuMemcpyDtoDAsync`, whose peer copies may execute through an SM kernel.

The paged path writes remote segments directly into their final attention locations:

$$\text{KPage}, \text{VPage} \in \mathbb{R}^{2 \times L \times N_{\max} \times n_{\text{head}} \times d_{\text{head}}}. \tag{13}$$

The leading dimension double-buffers rounds, and $N_{\max}$ bounds context tokens. Consumers fill anchor, retained history, and self slots, while producers fill legal remote slots. Attention reads the resulting ordered prefix without per-layer remote `torch.cat`. Here, "paged" means fixed-slot placement and does not eliminate local/history copies. Outgoing copies complete before the round boundary permits reuse, and generation flags distinguish successive uses of a slot.

B.3 Round schedule and cache semantics

Algorithm 1 implements the coordinates and active set defined in Sec. 3. It runs $N_{\text{chunk}} + S$ rounds, including fill/drain. The latent All-Gather at each round boundary remains in the asynchronous implementation and is distinct from the removed per-layer K/V collective.

Context order is exactly Eq. (5): anchor, bounded clean history, live store, self, then cleaner denoising slots in increasing stage order. The live store page becomes retained history after the round, avoiding a second steady-state broadcast. The first clean chunk serves as a persistent anchor, with its unrotated key retained so RoPE can be reapplied when the bounded window shifts. Other pages reuse their stored RoPE-applied keys.

Store processes B_{k-S} at the configured `context_noise` timestep, discards its prediction, and keeps each layer's K/V. This timestep is specified independently of S. Store attends to its anchor, retained history, and self. Its history budget reserves one query chunk, whereas denoising ranks reserve S chunks, so their prefix lengths can differ despite sharing the same clean-page list. Refresh timestep, prefix budgets, positions, and promotion order are part of the fixed semantics.

Conditioning, attention pages, and VAE convolution caches are request-local. The resident launcher handles one queued request at a time.

B.4 Output cadence, work, and fill/drain

Let T_s be stage s's local service time and T_{store} the clean-refresh time, measured for a specified graph, context, and backend. Sequential generation has period

$$T^{(S)}_{\text{serial}} = \sum_{s=0}^{S-1} T_s + T_{\text{store}}, \qquad T^{(1)}_{\text{serial}} = T_0 + T_{\text{store}}. \tag{14}$$

With $S+1$ stage-owned replicas, the filled wave period satisfies

$$T^{(S)}_{\text{wave}} \geq \max\{T_0, \ldots, T_{S-1}, T_{\text{store}}\}, \tag{15}$$

with equality only if communication and synchronization are fully covered. This permits an S-update pipeline to emit faster than serial one-step inference, but uses more replicas and does not reduce work or first-output latency. Across N_{chunk} chunks it still executes $N_{\text{chunk}}(S+1)$ full forwards. Structural slot occupancy is

$$\eta_{\text{slot}} = \frac{N_{\text{chunk}}}{N_{\text{chunk}} + S}. \tag{16}$$

All replicas are active only for $S \leq k < N_{\text{chunk}}$, so requests with $N_{\text{chunk}} \leq S$ never fill the pipeline. The 399-latent-frame workload has 133 chunks, giving $133/137 = 97.1\%$ slot occupancy at $S = 4$. First-output latency includes all denoising and store stages, VAE pipeline fill, and delivery.

B.5 Streaming VAE partitioning

Completed latents enter the decoder queue. Each latent-frame microbatch traverses contiguous decoder stages in order, preserving per-request causal-convolution caches. Profiling M_{VAE} ordered units at representative streaming shapes gives service times τ^{VAE}_m. Dynamic programming chooses P_{VAE} partitions by

$$\min_{0=b_0<\cdots<b_{P_{\text{VAE}}}=M_{\text{VAE}}} \max_{1\leq p\leq P_{\text{VAE}}} \sum_{m=b_{p-1}+1}^{b_p} \tau^{\text{VAE}}_m. \tag{17}$$

This balances estimated local service, including costs missed by unit counts or FLOPs. Inter-stage delivery must also fit the arrival interval. In per-latent-chunk units, the steady decoded-output interval is approximately

$$T^{\text{E2E}}_{\text{emit}} \approx \max\left(T^{\text{WP}}_{\text{round}}, \max_p T^{\text{chunk}}_{\text{VAE},p}\right) + T^{\text{exposed}}_{\text{delivery}}, \tag{18}$$

where decoder service amortizes all frame microbatches in one chunk, and the last term counts residual delivery not already covered by overlap or the service terms. Slower decoding grows queues or triggers bounded-buffer backpressure. The model excludes fill/drain and file encoding. Tab. 8 reports profiling, while Fig. 4 illustrates the schedules.

B.6 Same-graph semantic preservation

Wave Forcing changes the model graph relative to RF. Once the WF graph is fixed, synchronized and asynchronous execution can be compared at the operator level.

Proposition 1 (Same-graph scheduling)**.** *Fix the model parameters, denoising schedule, initial noise, per-update re-noising draws, text conditioning, positional embeddings, and history/store rules. Assume each local operator evaluates the same mathematical function and every attention operation receives the ordered K/V context in Eq.* (5)*, after the corresponding K/V production and delivery have completed. Then dependency-respecting asynchronous execution and synchronized execution produce the same mathematical latent sequence.*

Proof.

At the first tick, both executions start from identical inputs and empty history. At each layer, local Q/K/V projections depend only on that rank's current hidden states and fixed conditioning. The synchronized execution gathers all projections before consuming them. The asynchronous execution may publish and consume them at different times, but the readiness condition guarantees the same legal K/V values and sequence order at attention. Consequently each attention result and the remaining local layer outputs

agree. Induction over layers gives identical clean-latent predictions, from which the fixed scheduler and noise draws produce identical stage outputs. Store receives the same clean latent, runs the same cache-refresh computation, and promotes the same pages after the tick. Induction over ticks establishes identical histories and emitted latents through fill, steady state, and drain. □

B.7 Timing contract and multiple producers

On a common time base, let t_v^{local} be consumer $v = C_{k,s,\ell}$'s local-input/compute-stream ready time before remote waits. For each required edge e, set $t_e^{\text{need}} = t_v^{\text{local}}$ and $t_e^{\text{arrive}} = t_e^{\text{ready}} + \tau_e$. Eq. (11) then gives

$$t_v^{\text{start}} = \max\left(t_v^{\text{local}}, \max_{e \in \text{In}_{\text{KV}}(v)} t_e^{\text{arrive}}\right), \qquad w_v = t_v^{\text{start}} - t_v^{\text{local}} = \max_{e \in \text{In}_{\text{KV}}(v)} w_e. \tag{19}$$

The incoming set includes all legal cleaner ranks and active store. When it is empty, $t_v^{\text{start}} = t_v^{\text{local}}$ and $w_v = 0$. Earlier waits already affect these timestamps. Round critical paths additionally include transfer serialization, contention, and the boundary collective. Summing concurrent durations would double-count overlap. Measuring this contract requires correlated timestamps across calibrated device clocks, not just aggregate rank times.

B.8 Bounded attention storage and communication

The two K/V arrays in Eq. (13) have fixed capacity for anchor, bounded history, live store, and at most S denoising chunks, so attention-page storage is independent of generated video length. This bound excludes model weights and other request state. Explicitly retained video context is limited to the anchor and recent history.

For direct publication at steady state, denoising rank j sends its K/V chunk to j noisier ranks, for $S(S-1)/2$ payload destinations among denoising stages per layer. Store adds S destinations within the full wavefront. This quadratic count in S covers logical payload copies, while physical link traffic depends on transport and topology. The practical gain is reduced exposed communication under the timing condition in Eq. (11).

Index conventions. Chunk, denoising-stage, and rank indices are zero-based, whereas Transformer layers and VAE partitions are one-based. Diagram cells are tasks, whereas $Z_i^{(s)}$ is an input state. A round is a logical unit with variable wall time. Tab. 3 summarizes the graph-specific symbols, with local timing and shape variables defined alongside their equations.

Table 3: Graph and runtime notation. The complete wavefront includes store, whereas the denoising subset does not.

Symbol	Meaning
N_{chunk}, i	N_{chunk} is the number of requested chunks, and i indexes chunks with $0 \le i < N_{\text{chunk}}$.
S, s, ν_s	S is the number of denoising updates, s indexes denoising stages with $0 \le s < S$, and ν_s is the diffusion timestep. Store occupies execution stage $s = S$.
k, r	k indexes forward rounds, and r indexes diffusion ranks with $0 \le r \le S$, where rank S is Store.
$Z_i^{(s)}, B_i$	$Z_i^{(s)}$ is the state after s updates, and $B_i = Z_i^{(S)}$ denotes the clean endpoint.
$\mathcal{A}_k, \mathcal{F}_k$	active denoising-stage indices and their input states
$\mathcal{W}_k$	complete wavefront state, including the clean input to store when active
$C_{k,s}^{\text{WF},\ell}$	Ordered K/V context, with $k = i + s$ relating the round-based and chunk-based notation.
$A_k^\ell, H_k^\ell, U_k^\ell$	anchor, bounded clean-history, and live store K/V sequences
$P_{k,s,\ell}, C_{k,s,\ell}$	$P_{k,s,\ell}$ denotes Q/K/V production, and $C_{k,s,\ell}$ denotes attention and the remaining block tasks.

C Evaluation details

VBench protocol. We follow the standard VBench benchmark (Huang et al., 2024) with the original prompts, normalization, and weights, and scale scores to 0–100. For detailed metric definitions, we refer readers to the VBench paper. All metrics are computed with the official standardized evaluation scripts.

VBench-Long protocol. We report the VBench-Long Quality score and Dynamic Degree, scaled to 0–100. Each method uses the same 200 MovieGen prompts and seed 42, generating 399 latent frames and

saving 1593 frames (about 100 seconds) at 16 FPS per video. Causal Forcing (Full Attn.) uses the EMA generator of the released `chunkwise/longvideo.pt` checkpoint with its native 4-step schedule and full attention, for both standard VBench and VBench-Long.

Quality-generation setup. Rolling Forcing and Causal Forcing are evaluated in their own code repositories. RF with the causal mask and Wave Forcing use WaveRT with causal KV context, paged exchange, and a time-partitioned VAE. The 4-step and 5-step models use 4+1+3 and 5+1+2 GPUs, respectively, ordered as denoising + Store + VAE. Checkpoint quality is evaluated with SDPA for standard inference and SageAttention for fast inference. Execution performance is measured separately using FA3 and dummy DiT weights.

C.1 Long-video stability diagnostics

Prompt subset. Both diagnostics require a principal subject named in the prompt. A fixed text rule first removes, for every method, group scenes, scenery, first-person views without a stable visible subject, ambiguous principal entities, and prompts that ask the subject to disappear or transform. Of the 200 MovieGen prompts, 131 pass this rule. We then sample 100 of these prompts once at random and hold that subset fixed across methods, ablation studies, and both diagnostics. This subject-focused subset is distinct from the full 200-prompt VBench-Long evaluation.

Subject Preservation. We measure the prompt's principal-subject visibility.

SAM3 tracks the text-specified entity at 8 FPS, giving 797 sampled frames per video. The initial binding is the largest detection in the first eight frames, and masked DINO (Caron et al., 2021) features decide which later detections share that identity. Let A_t be the current mask area and A_0 the median mask area of the bound identity over the eight frames that begin at this binding. An associated box within 1% of the image border has visibility weight $\min(1, A_t/(0.18A_0))$, while any other associated detection has weight 1. A new instance elsewhere keeps its own track while the recognized subject still has weight at least 0.5 and mask area at least $0.18A_0$. Frames without an associated detection have weight 0. The video score is 100 times the mean weight over all sampled frames, including frames before the binding and frames without support. Videos that never receive an initial binding, and videos whose binding was reviewed as incorrect, are left unscored.

Camera Drift. Camera Drift measures persistent background motion with the subject moving toward an image boundary. We use the union of SAM3 detections for the text-specified entity at 8 FPS and point trajectories seeded outside those masks at 4 FPS. All distances are normalized by the image diagonal. For each image edge e, let g_e and q_e be the 5th and 90th percentiles of mask-pixel distances to that edge. Foreground outward velocity is the decrease in q_e divided by the 0.25-second pair duration. Background velocity is the component-wise median of per-cell median track velocities over supported spatial cells, projected onto the same outward axis. We apply $z(v) = \text{sign}(v)\max(|v| - 0.002, 0)$ to both velocities.

Within the preceding five seconds, we use pairs with observed foreground and background motion. For either corrected velocity sequence, define outward displacement $A = \max(0, 0.25\sum_t v_t)$, path length $P = 0.25\sum_t |v_t|$, and response $H = (A/P)A^2/(A^2 + 0.1^2)$, with $H = 0$ when $P = 0$. These give foreground and background factors F_e and B_e. Edge proximity is $E_e = \max(0, 1 - g_e/0.1)$. The instantaneous risk is $\max_e E_e F_e B_e$ over edges with positive current foreground and background velocities, or zero if no edge qualifies. Thus, background motion with a stationary subject does not incur a drift penalty.

To retain evidence after an exit, we require one second of consecutive outward foreground and background motion, at least two native pixels of foreground displacement, a final g_e within two native pixels of the boundary, and $q_e \leq 0.1$. After one second of consecutive explicitly empty masks, we hold the exit's $E_e F_e$ fixed and update B_e from current background observations, without backfilling the confirmation interval. Missing background tracks can be replenished by points consistent with the existing motion layer, but new points contribute only after tracking through a subsequent pair. This is a geometric association, not an independent semantic background label. A returning detection, uncertain mask, or scene cut ends the extension. Stopped or reversed background motion immediately gives zero risk and ends the extension after one consecutive observed second. Background gaps remain unscored, and later continuation is distinguished from uninterrupted support.

The video score is 100 times the mean risk over valid 0.25-second intervals, so lower is better. Startup intervals before five seconds, unavailable current measurements, and windows crossing a detected or unresolved cut remain unscored. Missing motion within a window is neither interpolated nor extrapolated. We average video scores equally over the prompt subset, requiring at least 20 scored seconds per video and using each method's own valid intervals.

C.2 Complete performance measurements

Tables 4 and 5 provide the WaveRT measurements plotted in Fig. 7a,b, including matched DiT/E2E rates in Tab. 4. Table 6 reports DiT throughput for each model scale, backend, and parallel strategy in Fig. 7c–f.

Experiment groups. Tables 4, 5, and 7 draw from the same fixed-three-repeat system sweep, reporting selected runtime configurations, pooled steady tick p50, and per-run ranges, respectively. Shared configurations report the same experimental runs. Table 6 is a separate DiT-only parallel-strategy sweep. Comparisons must respect each table's step counts, GPU allocations, timing scopes, and repetition cohorts.

Table 4: Runtime throughput. WaveRT uses the WF graph and paged K/V unless marked Sync, while Baseline is single-GPU rolling inference. Both use BF16 with FA3 unless a kernel suffix is specified. GPU counts include denoising, Store, and VAE: 4+1+3 for 4-step and 5+1+2 for 5-step. Speedup is E2E relative to the same-scale, same-step baseline. All rows use dummy DiT weights and a real-weight VAE. Best values are determined within each model/step group using unrounded measurements. DiT/E2E are paired.

Configuration	GPUs	Tick p50 (ms)	Steady (FPS)	DiT (FPS)	E2E (FPS)	Speedup
		1.3B, 4-step				
Baseline	1	–	–	33.86	19.06	1.00×
WaveRT (Sync)	8	91.96	130.50	129.31	127.06	6.67×
WaveRT	8	78.88	152.13	147.58	**134.81**	**7.07×**
WaveRT + Sage	8	78.36	153.15	**147.78**	134.79	7.07×
WaveRT + Sage + W8A8	8	**76.05**	**157.79**	145.47	132.89	6.97×
		1.3B, 5-step				
Baseline	1	–	–	29.12	17.46	1.00×
WaveRT	8	120.53	99.56	**104.82**	96.46	5.52×
WaveRT + Sage	8	**120.52**	**99.57**	104.80	**96.48**	**5.53×**
WaveRT + Sage + W8A8	8	120.59	99.51	103.49	95.15	5.45×
		14B, 4-step				
Baseline	1	–	–	6.31	5.51	1.00×
WaveRT (Sync)	8	464.27	25.85	25.56	25.47	4.62×
WaveRT	8	413.80	29.00	28.74	28.64	5.20×
WaveRT + Sage	8	414.03	28.98	28.72	28.62	5.19×
WaveRT + Sage + W8A8	8	**354.45**	**33.86**	**33.64**	**33.50**	**6.08×**

Table 5: WaveRT same-graph system ablations report pooled steady tick p50 (ms, lower is better) for the 4-step, 8-GPU (4+1+3) setup across three fixed repeats. Each row compares execution strategies under a fixed compute backend. All runs use dummy DiT weights and a real-weight VAE and measure execution cost only.

Backbone	Compute	Sync	Overlap	One-sided	Staggered	Paged
1.3B	BF16	91.956	85.730	81.669	81.953	**78.882**
1.3B	Sage	91.441	84.103	80.934	81.062	**78.356**
1.3B	Sage+W8A8	88.714	81.595	78.030	78.081	**76.052**
14B	BF16	464.270	449.689	425.907	425.188	**413.795**
14B	Sage	467.526	439.988	426.215	425.601	**414.029**
14B	Sage+W8A8	407.215	379.576	365.922	366.697	**354.447**

C.3 Runtime implementation and measurement protocol

The WaveRT runtime sweep uses one NVLink-connected node with eight H200 141-GB GPUs, 832 × 480 resolution video, and three latent frames per chunk. We implement WaveRT using Python 3.12, PyTorch 2.11.0+cu128, and SGLang Diffusion.

For the WaveRT measurements in Tabs. 4 and 5, each repetition generates 399 latent frames and 1593 decoded frames after a 399-latent-frame warmup. System FPS is 1593 divided by the median elapsed time across three fixed repetitions. Tick p50 pools steady-state ticks across those repetitions, and steady

Table 6: DiT throughput across parallel strategies and compute backends, using dummy DiT weights with VAE disabled. Step counts and GPU counts are matched across methods within each row. FPS is the arithmetic mean of per-run rates, and best values are determined using unrounded measurements. WP/CP divides WP throughput by that of the faster CP baseline. Amber † marks supplemental measurements whose repetition and stopping protocols are described in Appendix D.2.

				DiT throughput (FPS) ↑			
Scale	Compute	Steps	GPUs	Ulysses CP	Ring CP	WP	WP/CP
1.3B	BF16	5	6	80.60	41.19	**150.09**†	1.862×†
1.3B	Sage	5	6	84.01	56.99	**151.15**	1.799×
1.3B	Sage+W8A8	5	6	61.17	45.96	**154.75**	2.530×
3B	BF16	5	6	75.38	38.20	**88.86**	1.179×
3B	Sage	5	6	75.93	37.00	**89.26**	1.176×
3B	Sage+W8A8	5	6	56.15	36.04	**95.31**	1.697×
5B	BF16	5	6	58.40	41.42	**68.33**	1.170×
5B	Sage	5	6	63.13	30.37	**67.00**	1.061×
5B	Sage+W8A8	5	6	60.71	31.17	**75.44**	1.243×
7B	BF16	5	6	49.89	38.96	**53.28**	1.068×
7B	Sage	5	6	52.70†	25.75	**53.50**†	1.015×†
7B	Sage+W8A8	5	6	56.12	26.56	**61.55**	1.097×
9B	BF16	5	6	**46.41**†	38.94	45.70†	0.985×†
9B	Sage	5	6	45.26	22.73	**45.59**	1.007×
9B	Sage+W8A8	5	6	52.51	24.16	**53.84**	1.025×
14B	BF16	4	5	26.72	23.90	**28.71**	1.075×
14B	Sage	4	5	27.90	16.32	**28.72**	1.029×
14B	Sage+W8A8	4	5	30.98	17.16	**33.60**	1.085×

FPS is 12000/tick p50 (ms), using 12 decoded-equivalent frames per steady chunk. DiT timing covers pipeline fill and drain and may be affected by concurrent VAE decoding, while E2E timing additionally includes the remaining time until VAE completion. Loading and file encoding are excluded. The BF16 configuration uses FA3 self-attention. Both Sage configurations use SageAttention for self-attention and FA3 for cross-attention, with W8A8 linear computation enabled in the Sage+W8A8 configuration.

All new 1.3B and 14B system tests use dummy DiT weights and a real-weight VAE to evaluate execution cost, not generation quality. The 14B tests use the standard Wan2.1-T2V-14B architecture.

C.4 Throughput accounting and repeatability

Tab. 4 reports steady, complete-request DiT, and E2E rates together for each runtime configuration. Fill/drain and decoder service explain why these rates are not interchangeable. In particular, the lowest 1.3B tick p50 (WaveRT + Sage + W8A8) does not yield the highest E2E FPS.

Output-path limits in 5-step generation. Under the 8-GPU budget, 5-step WaveRT assigns five GPUs to denoising, one to Store, and two to a two-stage VAE pipeline (PP2), compared with three VAE stages in the 4-step setup. In the 5-step system measurements, BF16 and SageAttention achieve 104.82 and 104.80 DiT FPS, while E2E rates are 96.46 and 96.48 FPS, respectively (Tabs. 1 and 4). VAE concurrency is a plausible limiter under the smaller decoder budget, but system DiT timing can itself include concurrent decoder effects. These aggregate measurements do not isolate backpressure or establish a large hidden SageAttention speedup (Sec. 7).

The same-graph transport ablation (Fig. 7b and Tab. 5) compares Sync with asynchronous delivery. Tab. 7 reports the minimum and maximum per-run tick p50 across three repetitions on the same node for causal 4-step, 8-GPU WaveRT. These ranges summarize the same experimental runs as the matching configurations in Tabs. 4 and 5, while Tab. 6 reports a separate DiT-only sweep.

C.5 Mechanism diagnostics

Tab. 8 reports component-level profiles. The 38.32-ms difference compares aggregate forward intervals of the critical rank and the mean of other ranks, not per-layer readiness slack (Appendix B.7). BF16 and FP8 collective diagnostics are 58.45 and 31.23 ms per tick, excluding FP8 conversion, while one-sided and paged context assembly measure 19.02 and 5.91 ms per tick in separate profiling runs. The P2P

Table 7: Minimum–maximum of per-run tick p50 (ms) across three fixed repetitions on the same node for causal 4-step, 8-GPU WaveRT with dummy DiT weights. These ranges are not confidence intervals.

Scale	Compute	Sync	Overlap	One-sided	Staggered	Paged
1.3B	BF16	91.946–92.009	85.659–85.763	81.589–81.744	81.842–82.107	78.851–78.967
1.3B	Sage	91.390–91.462	84.035–84.168	80.933–80.953	80.806–81.235	78.290–78.400
1.3B	Sage+W8A8	88.579–88.781	81.505–81.634	77.975–78.099	77.895–78.291	75.769–76.284
14B	BF16	463.785–464.761	449.001–450.082	425.517–426.670	424.276–425.844	413.094–414.374
14B	Sage	466.946–468.320	439.004–440.453	425.819–426.635	425.420–425.753	413.711–414.304
14B	Sage+W8A8	407.121–407.384	379.268–380.479	365.482–366.516	366.552–367.034	354.189–354.720

Table 8: Diagnostic-only component profiles of stage service, K/V transfer, receiver-side assembly, and VAE partitioning, using three-run means. Each row reports a component timing within its stated measurement scope. Because these components can overlap during execution, their durations cannot be summed to obtain E2E latency. The producer range spans rankwise means.

Diagnostic	Measurement	Value
14B critical consumer	r0 forward interval	414.23 ms
14B producers	r1/r2/r3/store forward interval	370.50–379.37 ms
Aggregate rank-time difference	Critical minus mean of other ranks	38.32 ms
BF16 K/V communication	Rank 0 collective time summed over layers	58.45 ms
FP8 K/V communication	Payload and scale transfer, excluding conversion	31.23 ms
Copy-engine P2P	95,846,400-byte IPC copy	391.49 GB/s
Context assembly	One-sided to paged	19.02 to 5.91 ms
VAE FLOP-based split	Maximum isolated segment per chunk	115.76 ms
VAE time-based split	Three isolated segments per chunk	73.15 / 60.91 / 80.89 ms

rate is in decimal GB/s. These components can overlap with computation, so their E2E impact depends on exposed waits rather than the sum of their durations. The VAE split diagnostics report 115.76 ms for the slowest FLOP-based segment and 73.15/60.91/80.89 ms for time-based segments. Because the VAE segments are profiled sequentially on one GPU without inter-GPU transfers or queue waits, these measurements characterize isolated segment latency rather than online VAE capacity.

Transport correctness. Earlier checks of the 1.3B, 4-step configuration found that synchronized, one-sided, and paged execution of the same WF graph produced bit-identical latent outputs (`torch.equal=True`, zero maximum absolute difference). Same-graph scheduling equivalence is established in Appendix B.6.

C.6 Exposed communication, synchronization, and payload size

WaveRT targets time exposed on the consumer's critical path, not only bytes on the link. Early publication overlaps delivery with computation. One-sided writes replace matching collective coordination with point-of-use readiness checks, and paged placement avoids rebuilding remote context. Together, these changes reduce exposed communication, synchronization, and destination-assembly costs without eliminating data dependencies. At fixed BF16 computation, the 4-step 14B Sync/Overlap/One-sided/Paged tick p50 values are 464.270, 449.689, 425.907, and 413.795 ms (Tab. 5).

Payload size determines how much delivery must fit under computation. One chunk sent to one consumer at one layer carries $m_e(b) = 2N_C n_{\text{head}} d_{\text{head}} b$ bytes, with b bytes per element. Larger K/V width increases each payload, while more layers and destinations increase round traffic (Appendix B.8). Fixed hardware has unchanged peak link capacity, but effective bandwidth varies with topology and contention. Taking unquantized K/V readiness as the reference, a simple usable-delivery model is

$$\widetilde{\tau}_e(b) \approx t_e^{\text{quant}} + \alpha_e + \frac{m_e(b)}{B_e^{\text{eff}}} + t_e^{\text{dequant}}, \tag{20}$$

where α_e covers queueing and signaling, and B_e^{eff} is achieved payload bandwidth. BF16 requires no conversion, whereas FP8 halves payload bytes, excluding metadata, at the cost of conversion. With unchanged local timing, a previously exposed dependency can become hidden if

$$\widetilde{\tau}_e(1) \le \Delta_e < \widetilde{\tau}_e(2). \tag{21}$$

Every required edge, including store, must meet its deadline: local *attention* readiness, not projection start. Quantization can change execution timing, so actual slack must be measured per configuration.

The component profiles in Tab. 8 illustrate reduced transfer volume with FP8 K/V and reduced receiver-side assembly with paged placement. FP8 conversion can offset transfer savings under SageAttention. In the paged backend sweep (Fig. 7e,f), K/V remains unquantized, while W8A8 changes local DiT linear computation. These configurations vary the local compute backend while retaining the same K/V transport precision.

D Comparison of Execution Designs

D.1 Generation schedules and conditioning

Similar chunk–stage diagrams need not compute the same model. Tab. 9 distinguishes the state supplied to attention from the placement of work. All methods retain full within-chunk attention, but their weights, denoising schedules, and cache rules are method-specific.

Table 9: Conditioning and exchanged state in different generation schedules. Live K/V is produced by active chunks at the current Transformer layer.

Schedule	Context state	Across-stage transfer	Execution structure
Self Forcing	Completed clean-history K/V	None	Sequential chunks
Live Avatar	Fixed-timestep stage-local K/V snapshots	Updated latent	Stage pipeline
HiAR	Refreshed output-timestep K/V within each hierarchy	Updated latent	Causal hierarchy pipeline
Rolling Forcing	Clean history and bidirectional live K/V	All active K/V if distributed	Joint mixed-noise denoising
Wave Forcing	Clean history and causal live K/V	Cleaner-to-noisier K/V and latent	Directed wavefront

Sequential and joint-chunk generation. Self Forcing (Huang et al., 2025a) completes all updates of one chunk before starting the next, reusing clean-history K/V. Its bounded history cache can evict the initial chunk, whereas RF retains it as an anchor. RF (Liu et al., 2026) advances consecutive mixed-noise chunks jointly, emitting one clean chunk per joint call after fill. Distributed RF retains every active chunk's corresponding-layer K/V dependencies in both temporal directions. Communication overlap is still possible, but every consumer must respect those inputs. Both RF and WF are DAGs when unrolled over layers, so WF is distinguished by cleaner-only visibility, not merely by a topological order.

Stage-local and matched-noise pipelines. Live Avatar (Huang et al., 2025b) assigns a fixed denoising timestep to each process. Earlier stages retain their original K/V snapshots as a chunk progresses, and only latents move across stages. HiAR (Zou et al., 2026) instead builds a causal hierarchy: each level uses freshly produced K/V from earlier chunks at its output timestep ν_{s+1}. The cache write for chunk i can be fused with denoising chunk $i+1$. Its pipelined levels retain independent matched-noise caches and exchange latents, not layer-wise K/V between processes. This refreshed output-state context distinguishes HiAR from fixed-timestep snapshots.

Wavefront execution. WF preserves current-layer live K/V from all legal cleaner chunks and store, and WP publishes this K/V across full-model replicas. Thus an anti-diagonal schedule alone does not imply WF conditioning. Its causal mask, cache rules, and training establish the model, while publication and readiness checks implement it. Appendix B.4 gives the cadence and resource accounting without equating steady output rate with first-output latency.

D.2 Partitioning a forward versus distributing stages

Tensor and context parallelism partition one forward while retaining its conditioning graph. Ulysses (Jacobs et al., 2023) limits CP degree by attention-head divisibility, whereas Ring Attention (Liu et al., 2024) supports head-independent degrees through ordered K/V circulation. Synchronized chunk ownership keeps local queries and all their heads intact but retains Eq. (12)'s layer collective. WP instead relies on the WF graph and sufficient producer lead, at the cost of full-model replication.

Comparison setup. The three-backend comparison in Fig. 7c–f and Tab. 6 matches parameter count, backend tier, GPU count, and denoising-step count across methods within each model scale: a 5-step, 6-GPU setup for 1.3B–9B and a 4-step, 5-GPU setup for 14B. These rates are mean per-run DiT FPS with

Table 10: Resource-partitioning strategies, communication patterns, and constraints. TP and CP preserve the chosen graph, while WP schedules the fixed WF graph.

Method	Partitioned object	Main communication	Main constraint
Tensor parallelism	Hidden/head dimensions	Per-operator collectives	Small local GEMMs at high degree
Ulysses CP	Tokens to attention heads	Two All-to-All phases	Head divisibility and per-layer collectives
Ring Attention	K/V sequence blocks	Multi-round K/V circulation	Enough tile compute to hide P2P
Chunk-owned sync	Active query chunks	Layer K/V All-Gather	Global layer barrier
Wave Parallelism	Chunk–stage tasks	One-way K/V and latent	Full-model replicas and sufficient overlap slack

VAE disabled, whereas Fig. 7a reports E2E throughput for the 4-step, 8-GPU setup. Over the same rolling window, CP uses RF's full active-window attention, whereas WP uses WF's block-causal mask. The comparison therefore evaluates the combined effect of execution strategy and attention visibility. Tab. 10 summarizes how each strategy partitions work, communicates dependencies, and constrains resource allocation.

Model Configuration. The 1.3B and 14B models retain the standard Wan2.1 architectures. They share the same Wan Transformer block design but differ in the number of blocks, attention heads, hidden dimensions, and FFN dimensions. For the parameter-scale comparison in Tab. 6, we adjust these dimensions and the number of blocks to construct the intermediate 3B, 5B, 7B, and 9B architectures. Their attention-head counts are divisible by six to support six-way Ulysses parallelism. The standard 14B architecture has 40 attention heads and supports the five-way configuration used in our comparison. Tab. 11 lists all six configurations.

All six scales use dummy weights in the execution tests, including the standard Wan2.1-T2V-1.3B and 14B architectures. These tests measure execution performance separately from the trained 1.3B quality checkpoints. We do not train a 14B Wave Forcing model because the required computation exceeds our available resources.

Repetition protocol. Unmarked entries in Tab. 6 report the arithmetic mean of three fixed runs. The †-marked entries are supplemental diagnostics collected with throughput-based stopping.

Table 11: Model configurations for the parameter-scale comparison. The upper group contains the standard Wan2.1 architectures, and the lower group contains the synthetic architectures.

Parameters	Layers	Heads	Hidden dim.	FFN dim.
1.3B	30	12	1536	8960
14B	40	40	5120	13824
3B	32	18	2304	10752
5B	30	24	3072	14336
7B	29	30	3840	15360
9B	26	36	4608	18432

E Extended Future Work

This appendix develops the interaction, serving, and world-model extensions in Sec. 8, following the training and execution limits in Sec. 7. These extensions have not been evaluated with WF.

Online interaction and condition changes. LongLive (Yang et al., 2026) uses KV recaching to align visual context with an updated prompt; EditStream and LPM (Zhou et al., 2026; Zeng et al., 2026) explore interactive editing and character performance. A WF extension must specify which prompt applies to each active chunk, which cached states need refreshing, and whether outstanding work is completed or discarded. The fixed-context equivalence argument in Appendix B.6 does not establish correctness across condition changes. Sustained FPS and interaction delay are distinct: evaluation should measure when an input first changes the displayed video, as well as adherence and continuity.

Serving under streaming deadlines. StreamDiffusion's image-stream batching (Kodaira et al., 2025) and StreamDiffusionV2's video-stream scheduling (Feng et al., 2026) motivate deadline-aware batching around WF. SlackServe (Xia et al., 2026) relates scheduling and quality choices to buffered playback time, while PhysisServe's technical blog (Physis AI Infra Team, 2026) describes pipelining over transformer blocks and denoising steps, together with GPU time sharing. Future WF serving should study admission control, stream priorities, resource allocation, and finer-grained placement under its live-context dependencies. Changing sampling budgets also changes WP's available stage parallelism (Sec. 7); adopting another system's batching or state-reuse rules would therefore require checking WF's conditioning graph. Startup delay, output jitter, stall rate, and fairness should accompany throughput and quality measurements.

Learning controlled world evolution. One route extends video prediction with structured controls. minWM and ForgeWM (Zhao et al., 2026a; Li et al., 2026) study controllable few-step video generation; SolarWM (Huang et al., 2026a) emphasizes data standardization and causal adaptation; SANA-WM (Zhu et al., 2026a) explores hybrid linear attention for long-horizon generation; and OneWM (Su et al., 2026a) jointly learns world prediction and action generation. Integrating WF would require specifying when new camera or action inputs become available to in-flight chunks, validating state dependencies for each architecture, and assessing control fidelity, prediction consistency, and policy performance in closed-loop tasks.

Executable world state and generative rendering. A complementary route delegates persistent state, rules, and dynamics to code or an engine. Code World Model and Matrix-Game 4.0 (Chen et al., 2026; Zhang et al., 2026a) connect such state to video generation through visual proxies. StreamRender-H3 (Lu et al., 2026) and SolarRenderer (Fang et al., 2026) further motivate structure-conditioned streaming rendering. Here WF could supply an execution foundation for a renderer trained to follow incoming structure, rather than taking responsibility for the engine's dynamics. This would require aligned structure/video training and validation of temporal conditioning: StreamRender-H3 uses bidirectional attention within a streaming window, whereas SolarRenderer includes a block-causal variant. Neither establishes compatibility with WF's wavefront. Evaluation should check whether rendered observations preserve the underlying state and expose action effects quickly enough for feedback.

Understanding-assisted quality evaluation. Following the metric limits in Sec. 7, a future evaluator could combine local defect checks with long-horizon, instruction-aware judgments. StreamEval (StreamEval Team, 2026) evaluates timed requests and retained state alongside visual quality. StreamMeCo (Wang et al., 2026a) addresses efficient streaming video understanding, while MemForest (Wang et al., 2026b) provides event-centric memory compression and retrieval. These mechanisms could help a video-understanding judge retrieve temporal evidence about entities, actions, and failures. Adapting them to quality judging requires human-calibrated validation: we should report supporting timestamps and unscorable intervals, assess agreement with human annotations, and test whether compressed memory loses brief defects or earlier facts. The goal is to complement our targeted diagnostics with broader, auditable quality assessment.